Further evidence for CCN aerosol concentrations determining the height of warm rain and ice initiation in convective clouds over the Amazon basin

Ramon Campos Braga[1], Daniel Rosenfeld[2], Ralf Weigel[3], Tina Jurkat[4], Meinrat O. Andreae[5,9], Manfred Wendisch[6], Ulrich Pöschl[5], Christiane Voigt[3,4], Christoph Mahnke[3,8], Stephan Borrmann[3,8], Rachel I. Albrecht[7], Sergej Molleker[8], Daniel A. Vila[1], Luiz A. T. Machado[1], and Lucas Grulich[10]

[1] Centro de Previsão de Tempo e Estudos Climáticos, Instituto Nacional de Pesquisas Espaciais, Cachoeira Paulista, Brasil

[2] Institute of Earth Sciences, The Hebrew University of Jerusalem, Israel

[3] Institut für Physik der Atmosphäre, Johannes Gutenberg-Universität, Mainz, Germany

[4] Institut für Physik der Atmosphäre, Deutsches Zentrum für Luft- und Raumfahrt (DLR), Oberpfaffenhofen, Germany

[5] Multiphase Chemistry and Biogeochemistry Departments, Max Planck Institute for Chemistry, 55020 Mainz, Germany.

[6] Leipziger Institut für Meteorologie (LIM), Universität Leipzig, Stephanstr. 3, 04103 Leipzig, Deutschland

[7] Instituto de Astronomia, Geofísica e Ciências Atmosféricas, Universidade de São Paulo, Sao Paulo, Brazil

[8] Particle Chemistry Department, Max Planck Institute for Chemistry, 55020 Mainz, Germany.

[9] Scripps Institution of Oceanography, University of California San Diego, La Jolla, CA 92098, USA

[10] Institut für Informatik, Johannes Gutenberg-Universität, Mainz, Germany

Correspondence to: Ramon C. Braga (ramonbraga87@gmail.com)

Abstract: We have investigated how pollution aerosols affect the height above cloud base of rain and ice hydrometeor initiation and the subsequent vertical evolution of cloud droplet size and number concentrations in growing convective cumulus. For this purpose we used in-situ data of hydrometeor size distributions measured with instruments mounted on HALO aircraft during the ACRIDICON-CHUVA campaign over the Amazon during September 2014. The results show that the height of rain initiation by collision and coalescence processes (D_r, in units of meters above cloud base) is linearly correlated with the number concentration of droplets (N_d in cm^{-3}) nucleated at cloud base ($D_r \approx 5 \cdot N_d$). When N_d exceeded values of about 1000 cm^{-3}, D_r became greater than 5000 m, and the first observed precipitation particles were ice hydrometeors. Therefore, no liquid water raindrops were observed within growing convective cumulus during polluted conditions. Furthermore, also the formation of ice particles took place at higher altitudes in the clouds in polluted conditions, because the resulting smaller cloud droplets froze at colder temperatures compared to the larger drops in the unpolluted cases. The measured vertical profiles of droplet effective radius (r_e) were close to those estimated by assuming adiabatic conditions (r_{ea}), supporting the hypothesis that the entrainment and mixing of air into convective clouds is nearly inhomogeneous. Secondary activation of droplets on aerosol particles from biomass burning and air pollution reduced r_e below r_{ea}, which further inhibited the formation of raindrops and ice particles and resulted in even higher altitudes for rain and ice initiation.

1. Introduction

Understanding cloud and precipitation forming processes and their impacts on the global energy budget and water cycle is crucial for meteorological modeling. Therefore, many studies have focused on improving cloud parameterization in numerical weather and climate models (e.g., Frey et al., 2011; Khain et al., 2005, 2000; Klein et al., 2009; Lee et al., 2007; Machado et al., 2014). These parameterizations need to represent in simplified form the complex chain of events that occur in clouds.

Cloud droplets form when humid air rises and becomes supersaturated with respect to liquid water. Then water vapor condenses onto surfaces provided by pre-existing cloud condensation nuclei (CCN, a list of abbreviations and symbols is given in Table 1) aerosols. For ice formation, the ambient temperatures must reach values lower than 0 °C. At temperatures between 0 ºC and -36 ºC, ice in convective clouds mostly forms inhomogeneously on ice nuclei (IN) aerosols, often when they interact with supercooled liquid water droplets (Pruppacher et al., 1998). At colder temperatures (less than -36 ºC), cloud particles freeze due to homogeneous ice nucleation (Rosenfeld and Woodley, 2000).

A cloud predominantly consists of droplets with diameters larger than about 3 μm, except for transient smaller sizes right at cloud base. The number concentration of cloud droplets (N_d in cm^{-3}) at cloud base mainly depends on the conditions below cloud base, i.e., the updraft wind speed (W) and the supersaturation (S) activation spectra of cloud condensation nuclei [$CCN(S)$] (Twomey, 1959). In very clean conditions, values of N_d near cloud base are in the range of ~50-100 cm^{-3}, while in polluted condition N_d may reach values between 1000-2000 cm^{-3} (Andreae, 2009; Rosenfeld et al., 2008, 2014a).

Below the freezing level, raindrops are formed due to cloud droplet coagulation (collision-coalescence) processes (warm rain process). Mixed phase precipitation results from interactions between ice particles and liquid water droplets (Pruppacher et al., 1998). Several studies based on aircraft, radar and satellite measurements support that warm rain formation requires that the cloud consists of droplets with values of the effective radius (r_e) larger than 13-14 μm (Freud and Rosenfeld, 2012; Konwar et al., 2012; Prabha et al., 2011; Chen et al., 2008; VanZanten et al., 2005; Pinsky and Khain, 2002; Gerber, 1996; Rosenfeld and Gutman, 1994).

The effects of aerosol particles on clouds and precipitation have been studied in different parts of the globe (e.g., Fan et al., 2014; Li et al., 2011; Ramanathan et al., 2001; Rosenfeld and Woodley, 2000; Rosenfeld et al., 2014a; Tao et al., 2012; Voigt et al., 2017; Wendisch et al., 2016). A particularly interesting region is the Amazon basin, which presents contrasting environments of aerosol particle concentration between dry and wet seasons as well as steep aerosol concentration gradients within regions with near-constant thermodynamic conditions (Andreae et al., 2004; Artaxo et al., 2013). The background number concentrations of aerosol particles and CCN over the pristine parts of the Amazon region are about a factor of 10 times lower than those of polluted continental regions, including polluted conditions over the Amazon (Martin et al., 2016). During the dry-to-wet transition season in the Amazon region, total aerosol number concentrations reach values up to 10,000 cm^{-3}, mostly due to forest fires (Andreae, 2009; Andreae et al., 2012; Artaxo et al., 2002). On the other hand, in the rainy season aerosol number concentrations are about 500-1000 cm^{-3} with CCN concentrations on the order of 200-300 cm^{-3} for 1 % supersaturation, mainly consisting of forest biogenic aerosol particles (Artaxo, 2002; Martin et al., 2016; Pöhlker et al., 2016; Pöschl et al., 2010). Additionally, Manaus city, which is located at the central Amazon basin, releases significant concentrations of urban pollution aerosol particles (e.g., due to traffic, combustion-derived particles, or different types of industrial activities). This increases CCN concentrations by up to one order of magnitude (for 0.6% supersaturation) from the wet (Green Ocean) to the dry season (Kuhn et al., 2010).

Rosenfeld et al. (2012b) showed that by estimating the adiabatic number of droplets nucleated at cloud base (N_a), the height above cloud base at which the first raindrops evolve can be parameterized. This approach is based on the assumption that the entrainment and mixing of air into convective clouds is almost completely inhomogeneous (Beals et al., 2015; Burnet and Brenguier, 2007; Freud et al., 2011; Paluch, 1979). This implies that the vertical profile of the actual cloud droplet effective radius behaves nearly as in an idealized adiabatic cloud. This connects uniquely the adiabatic drop number concentration, which is approximated by N_a at cloud base, with the adiabatic droplet effective radius (r_{ea}), based on an adiabatic parcel model for which droplet growth is dominated by condensation (Freud and Rosenfeld, 2012; Pinsky and Khain, 2002). This parameterization can be applied to estimate the height above cloud base at which raindrops start to form, when r_{ea} reaches 13 μm (D_{13}) [Freud and Rosenfeld, 2012; Konwar et al., 2012; Rosenfeld et al., 2012b; Prabha et al., 2011; VanZanten et al., 2005]. However, uncertainties associated to the calculated N_a decrease the agreement between r_{ea} and r_e. Most of these uncertainties arise when secondary activation of droplets happens above cloud base because the adiabatic model does not predict that N_d increases with height, but decrease due to evaporation and inhomogeneous cloud mixing (Pinsky and Khain, 2012).

Braga et al. (2016) applied the methodology described by Freud and Rosenfeld (2011) to calculate N_a at the base of growing convective cumulus clouds for the Amazon region during the ACRIDICON-CHUVA (Aerosol, Cloud, Precipitation, and Radiation Interactions and Dynamics of Convective Cloud Systems)-CHUVA (Cloud processes of tHe main precipitation systems in Brazil: A contribUtion to cloud resolVing modeling and to the GPM [Global Precipitation Measurements]) campaign (Wendisch et al., 2016). The N_a is calculated from $N_a = CWC_a / M_{va}$, where CWC_a is the adiabatic cloud water content (CWC_a) as calculated from cloud base pressure and temperature, and M_{va} is the adiabatic mean volume droplet mass, as approximated from the actually measured mean volume droplet mass (M_v) by the cloud probe DSDs obtained during the cloud profiling measurements. Measurements of M_v with height are considered only for cloud passes where CWC is greater than 25 % of the adiabatic CWC and r_e is lower than 11 μm (i.e. for cloud droplets which have grown mostly via condensation). The calculated N_a based on the measured vertical profile of r_e agreed well (within 20-30 %) with the actual measurements of cloud droplet number concentrations at cloud base. This approach provides the opportunity to test the agreement between estimated r_{ea} and the height above cloud base of warm

rain initiation (D_r) within clouds for the Amazon region. In addition, measurements of the height above cloud base of ice initiation (D_i) in convective clouds are also available from flights that include cloud penetrations at ambient temperatures as low as -60 ºC with the HALO aircraft (Wendisch et al., 2016).

This study analyzes the vertical development of cloud and precipitation particles (water drops and ice crystals) in growing convective cumulus over the Amazon, based on measurements of cloud microphysical properties from instruments mounted on HALO during ACRIDICON-CHUVA (Wendisch et al., 2016). The vertical profile of r_{ea} is used to estimate the depth above cloud base at which warm rain initiation occurs. The dominance of inhomogeneous mixing causes the r_e profile to behave almost as in adiabatic clouds, constrained by N_d at cloud base (Burnet and Brenguier, 2007; Freud et al., 2011). This means that the height above cloud base for reaching r_e of 13-14 μm, which is required for rain initiation, is also determined by cloud base N_d (Freud and Rosenfeld, 2012). Rain initiation depends strongly on r_e because the rain production rate by collision and coalescence is proportional to ~r_e^5 (Freud and Rosenfeld, 2012). Here we test and quantify these relationships for the measurements conducted with HALO during ACRIDICON-CHUVA.

The HALO flights during the ACRIDICON-CHUVA campaign were performed over the Amazon region under various conditions of aerosol concentrations and land cover (Wendisch et al., 2016). Figure 1a shows the flight tracks during which cloud profile sampling in growing convective cumulus was performed. Figure 1b shows a schematic sketch of the flight pattern while sampling cloud clusters (the locations in three dimensions of each flight are available at Figure 1 on supplementary material). The aircraft obtained a composite vertical profile by penetrating young and rising convective elements, typically some 100-300 m below their tops.

The cloud droplet size distributions (DSDs) between 3-50 μm diameter were measured at a temporal resolution of 1 second by the CAS-DPOL and CCP-CDP probes (Baumgardner et al., 2001; Lance et al., 2010; Brenguier et al., 2013). Each DSD spectrum represents 1 s of flight path (covering ~150 m of horizontal distance for a typical aircraft speed). The value of r_e was calculated for each 1-s DSD. The two probes (CAS-DPOL and CCP-CDP) were mounted on opposite wings of HALO (horizontal distance of ~15 m). Similar values of N_d and derived r_e were measured by CAS-DPOL and CCP-CDP (they agree within 30 %), even though they were mounted on different wings. A previous study (Braga et al, 2016) showed that both probes were in agreement within the measurement uncertainties with respect to the measured cloud droplet number concentrations at cloud base and in accordance with the expected values for different conditions of CCN concentration and updraft wind speed below cloud base. In addition, the CWC calculated from the measured DSDs shows similar values to those measured with a hot wire device for different heights above cloud base [the probes' measurements agree within their uncertainty range (16% for probe DSDs and 30% for hot-wire device)] (Braga et al., 2016).

The determination of the height of rain initiation is based on the drizzle water content (DWC) calculation from the CCP-CIP probe (Brenguier et al., 2013). The DWC is defined as the mass of the drops integrated over the diameter range of 75–250 μm (Freud and Rosenfeld, 2012). This size range is selected because it includes only drops with terminal fall speed of 1 m s^{-1} or less, which maximizes the chance that the drizzle was formed in situ and did not fall a large distance from above. Rainwater content (RWC) is defined as the CCP-CIP integrated liquid water mass of droplets with diameters between 250 and 960 μm. The CCP-CIP images were used to distinguish raindrops and ice particles during cloud passes. The hydrometeor type is identified visually by their shapes. The phase of the smaller CCP-CIP particles cannot be distinguished. Therefore, the precipitation is considered as mixed phase when ice particles are identified, and the combined DWC and RWC are redefined as mixed phase water content (MPWC). Table 2 summarizes the calculated cloud microphysical properties with respect to the instrumentation used and its size ranges.

2. Instrumentation

2.1 Cloud particle measurements

The instrumentation used to measure cloud particles and rain or ice formation consists of three cloud probes: CAS-DPOL, CCP-CDP and CCP-CIP (Brenguier et al., 2013). In this study, cloud particle counts are accumulated for bin diameters larger than 3 µm from the CCP-CDP and CAS-DPOL; the lower size bins from these probes overlap with haze particles. Nucleated cloud drops in convective clouds grow quickly beyond 3 µm. Details about the cloud probe measurements characteristics are described in the following sub-sections and in Braga et al. (2016).

2.2.1 CCP-CDP and CCP-CIP measurements

The Cloud Combination Probe (CCP) combines two detectors, the Cloud Droplet Probe (CDP) and the greyscale Cloud Imaging Probe (CIPgs). The CDP detects forward scattered laser light of cloud particles when penetrating the CDP detection area (Lance et al., 2010). The CIP records 2-D shadow cast images of cloud elements. In this study, we deduced the existence of ice from the occurrence of visually non-spherical shapes of the shadows. The particle detection size range is 2 µm to 960 µm when measuring with the CCP at 1 Hz frequency (Wendisch et al., 2016). The combination of CCP-CDP and CCP-CIP information provides the ability to measure cloud droplets and raindrops within clouds for nearly the same air sample volume. The maximum number of particles measured by CCP-CDP and CCP-CIP are about 2,000 and 500 cm^{-3} for 1 Hz cloud pass, respectively. For the data processing of the CIP measurements, ice is assumed as the predominant particle phase in the mixed-state cloud conditions throughout the ACRIDICON-CHUVA campaign. The assumption of ice density instead of water density implies a slight overestimation (~10 %) of the calculated rain water content for particles greater than 75 µm.

2.2.2 CAS-DPOL measurements

The CAS-DPOL measures particle size distributions between 0.5 and 50 µm at 1Hz time resolution (Baumgardner et al., 2011; Voigt et al., 2010; Voigt et al., 2011). Number concentrations are derived using the probe air speed measured at the instrument. Particle inter-arrival time analysis did not show influences of coincidence (Lance, 2012). The data analysis and uncertainties are described in detail in Braga et al. (2016).

Braga et al. (2016) have shown sufficient agreement between both CAS-DPOL and CCP-CDP measurements of cloud droplet number concentration to distinguish convective clouds that develop above clean vs. polluted regions during the ACRIDICON-CHUVA campaign. In addition, the CWC estimated by integration of the DSDs measured with both probes showed good agreement with hot wire CWC measurements (Braga et al., 2016).

2.3 Meteorological data

The HALO aircraft was equipped with a meteorological sensor system (BAsic HALO Measurement And Sensor System - BAHAMAS) located at the nose of the aircraft (Wendisch et al., 2016). The uncertainties for measurements of temperature, relative humidity and vertical wind speed are 0.5 K, 5 % and 0.3 m s^{-1}, respectively (Mallaun et al., 2015).

2.4 Aerosol measurements

Aerosol particle measurements were performed using the Passive Cavity Aerosol Spectrometer Probe 100X (PCASP-

100X), which is an airborne optical spectrometer that measures aerosol particles in the 0.1 μm to 3 μm diameter range (Liu et al., 1992). The maximum number of particles measured by PCASP is about 3,000 cm^{-3} for 1 Hz cloud pass. During ACRIDICON-CHUVA campaign PCASP was not operated with a heated inlet, thus, the measured aerosol particles below cloud base (about 200 m) can be larger than the original dry size due to swelling.

3. Methods

The analyses are performed along the following general steps:

a) The relationship between r_e and the probability of drizzle is defined. The value of r_e is calculated from the size distributions measured by the CAS-DPOL and the CCP-CDP (two different values). DWC, RWC, and MPWC are obtained from the CCP-CIP data.
b) The N_a at cloud base is estimated through the vertical profile of r_e.
c) The height of rain initiation based on the modeled adiabatic growth of r_e with height is estimated for different aerosol condition as a function of estimated N_a. The value of D_{13} is estimated as the cloud depth for which the adiabatic r_e reaches 13 μm.
d) The extent of agreement between the directly measured D_r within convective clouds and the estimated D_{13} based on the assumption of adiabatic r_e growth and on the measured r_e is discussed.

3.1. Estimation of r_e, rain and ice initiation

Rain is initiated during the warm phase of growing convective cumulus by intensification of the collision and coalescence (coagulation) processes with height. The efficiency of the process of droplet coalescence is determined by the collection kernel (K) of the droplets and their concentrations (Pruppacher et al., 1998). Freud and Rosenfeld (2012) have shown through model simulations and aircraft measurements that $K \propto r_v^{4.8}$, where r_v is the mean volume radius obtained from the cloud probe DSDs in the absence of ice. r_v is defined as follows:

$$r_v = \left(\frac{3\ CWC}{4\ \pi\ \rho\ N_d} \right)^{\frac{1}{3}} \qquad (1)$$

where ρ is the water density (1 g cm^{-3}), CWC is in g m^{-3}, and N_d is in cm^{-3}. The values are obtained from the 1-Hz data of droplet size distributions from the cloud probes. The calculation of CWC is performed separately with CAS-DPOL and CCP-CDP probe droplet concentrations as follows:

$$CWC = \frac{4\pi}{3} \rho \int N(r) r^3 \mathrm{d}r \qquad (2)$$

where N is the droplet concentration and r the droplet radius. The calculations of DWC, RWC, and MPWC are done in similar fashion to CWC but with different cloud probes and particle size ranges (see Table 2).

The definition of r_e is:

$$r_e = \frac{\int N(r) r^3 dr}{\int N(r) r^2 dr} \qquad (3)$$

Freud and Rosenfeld (2012) showed that $r_v \approx 1.08 \cdot r_e$, depending on the droplet size distribution. Using this relationship, they derived r_e from r_v and showed that warm rain initiates within clouds when r_e is about 13-14 μm (Klein et al., 2009; Rosenfeld and Gutman, 1994; Rosenfeld and Lensky, 1998; Rosenfeld et al., 2012a, 2014b).

Only measurements with CWC larger than 25% of the adiabatic water content are considered in order to exclude convectively diluted or dissipating clouds. It is assumed that rain (or ice) formation starts when calculated DWC exceeds 0.01 g m^{-3} (Freud and Rosenfeld, 2012). For rain initiation in liquid phase the DWC threshold is ~10% greater due to the overestimation of DWC during CIP measurements in warm clouds (as stated at Section 2.2.1). The small terminal fall speed of the drizzle drops (≤ 1 m s^{-1}) allows to focus on in-situ rain (or ice) initiation while minimizing the amount of DSDs affected by rain drops fallen from above into the region of measurements. In addition, cloud passes with rain were eliminated when cloud tops were visibly much higher than the penetration level (> ~1000 m), based on the videos recorded by the HALO's cockpit forward-looking camera. However, cloud tops higher than few hundred meters above the penetration level occurred only rarely.

Table 3 shows the cloud depth above cloud base at which warm rain initiation occurs (D_r) (i.e., DWC > 0.01 g m^{-3}) for all flights as a function of estimated N_a. The D_r is taken as the cloud depth for ice initiation (D_i) if ice particles are evident in the CCP-CIP images.

3.2. Estimating N_a and adiabatic r_e

The N_a for the convective clusters is estimated based on the slope between the calculated CWC and the mean volume droplet (M_v) for 1-s DSD measurements of CAS-DPOL and CCP-CDP for non-precipitating cloud passes (Braga et al., 2016). Braga et al. (2016) have shown that this estimated N_a was in a reasonably good agreement with the directly measured cloud base droplet number concentration, N_d, as obtained from the CCP-CDP and CAS-DPOL during ACRIDICON-CHUVA. Once N_a is estimated, the adiabatic r_e (r_{ea}) can be calculated based on a simple adiabatic parcel model where droplet growth is dominated by condensation (Pinsky and Khain, 2002).

The N_a calculated for cloud base was used to classify clouds as having developed in clean, polluted, or very polluted regions. A clean cloud case was defined as N_a < 500 cm^{-3}, polluted for 500 cm^{-3} < N_a < 900 cm^{-3}, and very polluted for N_a > 900 cm^{-3}. During ACRIDICON-CHUVA, a flight in clean clouds (AC19) was performed over the Atlantic Ocean. Clouds observed during flights over the northern Amazon were classified as polluted, mainly due to diluted smoke from biomass burning advected by long-range transport. This region represents the Amazon background condition for aerosol concentration during the dry season. Very polluted conditions were met over the Central Amazon, which was affected strongly by biomass burning over the Amazonian deforestation arc (southern Amazon).

4. Results

4.1 Threshold of r_e for warm rain initiation

The values of r_e derived from integrating the cloud probe DSDs were used to identify rain initiation. Some caution is required to eliminate possible bias resulting from peculiar shapes of the drop size spectrum. An r_e value of 13-14 μm represents the rain initiation threshold for growing convective cumulus observed at different locations in the world, as long as there is no significant influence from giant CCN (GCCN; dry soluble diameter > 1 μm) (Freud and Rosenfeld, 2012).The presence of GCCN during cloud droplet formation at cloud base can lead to a faster formation of raindrops due to both, the rain embryo effect and the competition effect that reduces cloud base maximum supersaturation and consequently reduces N_d (Rosenfeld, 2000; Segal et al., 2007). Such cases are very common over the ocean due to sea spray aerosols; there, the values of r_e at which raindrops start to form are commonly smaller than the usual threshold of

13-14 μm (Freud and Rosenfeld, 2012). In our study the DSDs from flight AC19 performed over the Atlantic Ocean did not show a large drop tail near cloud base (see Figure 2 in the supplementary material). The cumulative sample volume from CCP-CDP probe at cloud base was about 5.8 L^{-1} for 176 s of measurements. The figure shows the scarcity of large cloud droplet (with diameters > 20 μm) near cloud base, where the mean concentration of such droplets is smaller than 0.1 drop cm^{-3}. Such small concentration of large droplets at cloud base is insufficient to have any significant effect on supersaturation.

Figures 2a-b show the precipitation initiation probability as a function of r_e calculated from the CCP-CDP and CAS-DPOL probes for all flights analyzed over the Amazon. The precipitation probability is calculated by integrating the measured DSDs exceeding certain DWC thresholds. These figures show that for the CCP-CDP probe rain initiation is expected to occur at r_e > 13 μm, whilst for CAS-DPOL the rain initiation threshold is r_e > 12 μm. Difference of the two instruments in the r_e range below ~7 μm and above ~11 μm have been discussed in Braga et al. (2016). For r_e < 7 μm, they are related to a higher sensitivity of the CAS-DPOL for small cloud and aerosol particles, whereas for r_e > 11 μm CAS-DPOL has lower sensitivity to large particles than CCP-CDP; however the differences are not significant within the uncertainties of the measurements. According to Figure 3, the r_e calculated with the DSD measured with the CCP-CDP is about ~7% higher than the r_e calculated from CAS-DPOL data.

Figures 4a-b show the relationship between r_e and r_v calculated for both cloud probes. The figure shows slight differences between the probes, with $r_v \sim 1.065 \cdot r_e$ for CCP-CDP and $r_v \sim 1.085 \cdot r_e$ for CAS-DPOL [which is closer to what was found by Freud and Rosenfeld (2012), where $r_v \sim 1.08 \cdot r_e$]. The agreement between these probes and theoretical models, shown by Braga et al. (2016), supports their use for closure analysis between r_{ea} and r_e calculated from measured DSDs as a function of cloud depth above cloud base (D_c). Because the CCP-CDP was mounted very close to the CCP-CIP, results from this probe are shown in subsequent sections; similar results were found from data collected with the CAS-DPOL probe.

4.2 Comparing estimated r_{ea} with measured r_e

The comparison between the values of r_{ea} (calculated from the estimated N_a at cloud base described in Section 3.2) with the measured r_e is the basis for analyzing the evolution of cloud particle size until rain or glaciation initiation occurs within the cloud. Rosenfeld et al. (2012b) showed that a tight relationship between the N_a calculated for cloud base and the evolution of r_{ea} with height (r_{ea}-D_c) provides a useful proxy of the depth in convective clouds at which raindrops start to form.

4.2.1 Case study: Flight AC07 over the Amazon deforestation arc

Flight AC07 was performed over the deforestation arc (see Figure 1a). Figure 5 shows the number of droplets measured at different heights in the convective clouds. Droplet concentrations reaching ~2000 cm^{-3} were measured at cloud base, which is characteristic for very polluted clouds. The cloud base was located at about 1900 m above sea level, with ambient air temperature at about 16ºC. Figure 6a shows the mean DSD for a cloud penetration at cloud base. It emphasizes the higher number concentration of small droplets (< 10 μm) that are observed in convective clouds forming in polluted environments. Figure 6b shows the evolution of r_e measurements and estimated r_{ea} as a function of temperature. The figure also shows that the values of r_e do not exceed the 13 μm threshold at warm temperatures. These results suggest that cloud droplets formed at cloud base grow mainly via condensation and no raindrops were formed during the warm phase of convective cloud development. However, to rule out coalescence processes as a possible reason for droplet growth, further analysis using CCP-CIP images was done.

Figures 7a-c show the evolution of DSD and CWC (mean values) as a function of height above cloud base and the cloud particle images from the CCP-CIP. Figure 7a plots the data for a cloud pass at warm temperatures and Figures 7b-c result from measurements during cloud passes at cold temperatures. The DSDs show that most droplets have a diameter smaller than 20 µm, and only very few large droplets are observed for warm temperatures. The CCP-CIP detected only cloud droplets and no raindrops, as evident by both RWC and DWC < 0.01 gm^{-3}. At cold temperatures, the CCP-CIP images show the irregular shapes of large ice particles. No spherical raindrop shapes were found in these data for any of the cloud passes, including those collected at warm temperatures. The DWC and RWC calculated from the mean DSDs show values greater than zero only when ice particles were observed on the CCP-CIP images. Also, for a cumulative sample volume of 1.24 m^{-3} from 89 s of CCP-CIP measurements, no raindrop were observed between the heights above cloud base of 2,900 m (0ºC) and 7,100 m (-26.25 ºC). This means that the raindrop concentration, if any, was smaller than 1 drop m^{-3}. This is a negligible rain rate, and supports the notion of practical shut of coalescence. Furthermore, the CCP-CIP did not detect any raindrops at lower levels (warm temperatures) for a cumulative sample volume of 5.9 m^{-3} from 426 s of measurements. These results indicate a strong inhibition of raindrop formation within growing convective cumulus for this flight over the deforestation arc of the Amazon. Even though some of the indicated effective radii values are larger than 13 µm for colder temperatures, these values do not indicate rain formation when only ice particles are observed. This does not exclude the possibility that small raindrops froze soon after their formation in such low temperatures.

The mean DSD and CIP images shown in Figure 7c result from a passage through a convective cloud with lightning activity. Figure 8 shows a photo of the cloud taken from the HALO cockpit just before the cloud penetration. The CCP-CIP has imaged graupel in this case. The presence of these type of ice particles within convective clouds is very common in thunderstorms, and previous studies highlight the large frequency of lightning occurrence during the dry-to-wet season over the deforestation arc region of the Amazon (Albrecht et al., 2011; Williams et al., 2002). These results also highlight the role of aerosols from biomass burning on warm rain inhibition and on the aerosol invigoration effect due to the generation of large ice particles and lightning (Rosenfeld et al., 2008).

Regarding the values of r_e as a function of D_c, Figure 9a shows the estimated r_{ea} (calculated from the adiabatic CWC shown at Figure 9b) and measured r_e. The figure shows that the estimated values for r_{ea} are close to the r_e measurements for convective cloud passes at different D_c. Even though no raindrops were observed in the convective cloud, the figure shows similar values of r_{ea} and measured r_e (with r_{ea} slightly larger) as a function of D_c.

4.2.2 Analysis of r_e and D_c in clean and polluted regions

- Clean region

Figure 10a shows the measured N_d of a convective cluster over the Atlantic Ocean off the Brazilian coast (flight AC19). This region was classified as clean because N_a is about 300 cm^{-3} (see Table 3). The cloud base was located at 600 m above sea level at a temperature of 23 ºC. Given the clean conditions over the ocean, the high relative humidity at surface level and the low concentration of CCN lead to the formation of large droplets already close to cloud base. Figure 10b shows the estimated r_{ea} and the measured r_e as a function of D_c. Several cloud passes showed large droplets with r_e ~ 13 µm at only 1660 m above cloud base. Figures 11a-b show the DSDs and CCP-CIP images for the cloud passes at the height where rain starts to form and at the greatest height measured above cloud base, respectively. Figure 11a shows that rain is initiated (DWC > 0.01 g m^{-3}) already when the droplets become larger than about r_e > 12 µm. This is probably due to the presence of GCCN over this maritime region.

Figure 12 shows the mean aerosol particle size distribution (PSD), as measured by the PCASP, just below cloud base for clean, polluted, and very polluted regions. The mean total number concentration of aerosol particles with sizes larger than 0.1 μm is about 1000 cm^{-3} over the Atlantic Ocean, whilst for polluted (very polluted) case this value is about three (ten) times larger. In addition, the mean total number concentration of particles measured by the CCP-CDP show concentration ten times greater for particles larger than 10 μm over the ocean in comparison with inland Amazon region. This figure indicates the presence of large aerosols particles with sizes greater than 1 μm (possibly GCCN) over the ocean. When it nucleates droplets, this type of aerosol accelerates the growth of droplets during the warm phase leading to a faster formation of raindrops than predicted by the adiabatic parcel model. About 3500 m above cloud base, large raindrops are observed in the CCP-CIP images (see Figure 11b). The low CWC indicates that most of it was already converted into raindrops. These results highlight that under clean conditions, raindrops were formed mainly by warm phase processes of cloud development. Even if the convective clouds reach colder temperatures, the low remaining amount of cloud water reduced a key ingredient for cloud electrification.

Before raindrops start to form (*Dc* ~1,660 m) updrafts were observed with most values < 4 m s^{-1}, and when rain starts downdrafts starts to be evident (see Figure 3g at supplementary material). The values of vertical velocities measured at flight AC19 (clean region) were smaller than measured for flight AC07 (very polluted region). However, for both cases updrafts are more evident during droplets growth via condensation and downdrafts are stronger when precipitation particles are observed in the cloud. Strong updrafts (~10 m s^{-1}) are observed in polluted cases after ice starts to form, probably due to the latent heat release during freezing processes. An alternative explanation of updraft enhancement due to environmental conditions in these cases cannot be excluded.

-Polluted regions

The flights AC09 and AC18 were classified as polluted (see Table 3). These flights were performed over the northern Amazon region (see Figure 1a). Figure 13a shows the measured N_d from flight AC09. The cloud base was located about 1200 m above sea level at a temperature of 19.5 ºC. Figure 13b shows the estimated r_{ea} and the measured r_e as a function of D_c. Values of r_e > 13 μm were observed for temperatures around 0 ºC, indicating the possibility of rain starting at this height. Figure 14a-b shows the DSDs and CCP-CIP images from flight AC09 at the height where rain starts to form (D_r ~3000 m) and at the greatest height with measurements above cloud base. The CIP image at Figure 14b shows the first pass in which ice hydrometeors are observed mixed with supercooled rain drops. For lower levels only raindrops were observed. For flight AC18 cloud base was located about 1700 m above sea level at a temperature of 17 ºC, and rain started to form in convective clouds when D_r ~3800 m. Figure 5a at the supplementary material shows that first rain drops in AC18 are observed at the -5.7 ºC isotherm, and that they still remain liquid, or at least spherical, at the -11.4 ºC isotherm (see Figure 5b at the supplementary material). Larger raindrops and a high amount of DWC were observed on AC09 for warmer temperatures than on flight AC18 (not shown). These results show that differences in cloud particle formation are associated with the D_c at which convective clouds start to form raindrops or ice, defined earlier as D_r and D_i. Flight AC18 has a droplet concentration, N_d, of up to 100 cm^{-3} greater than the measurements during AC09. With higher N_d at cloud base, droplet growth via condensation in convective clouds is a less pronounced function of height due to the water vapor competition between droplets. Under these conditions, the collision and coalescence process and freezing of droplets are initiated at higher D_c (Freud and Rosenfeld, 2012; Rosenfeld et al., 2008). For this the reason, the formation of raindrops and ice particles on flight AC09 starts at lower D_c than on flight AC18 (assuming non-significant secondary drop activation above cloud base).

-*Very polluted regions*

Five flights were classified as very polluted (see Table 3): AC07, AC08, AC12, AC13, and AC20. The microphysical analysis of the measurements collected in growing convective cumulus during flight AC07 was already presented in Section 4.2.1. Figure 15a show the measured N_d from flight AC13, which was made in the same region as flight AC07. The figure shows that the values of N_d near cloud base on flight AC13 reach 2000 cm^{-3}, similar to AC07. However, the rate of decrease of N_d with height above cloud base is much smaller in AC13 compared to AC07. During flight AC13 the measurements of large updrafts (which increase supersaturation and induce new droplets activation) and large aerosol concentration above cloud base suggest the occurrence of secondary activation leading to the observed relative increase of N_d with height. This is supported by the fact that the observed r_e are smaller than the calculated r_{ea}, as shown in Figure 15b. Only values below 13 µm are observed (maximum of 12 µm), indicating the suppression of raindrop formation. Indeed, no raindrops were observed in the CCP-CIP images from growing convective cumulus passes on this flight, and only cloud droplets and ice particles were detected. Figure 16 shows the DSD and CCP-CIP images at the start of glaciation (D_i ~4800 m). These results highlight the role of aerosols in inhibition of raindrop formation due to inducing a larger N_d and respective lower r_e, which leads to suppression of collision and coalescence processes in very polluted regions.

The measured N_d during flights AC08, AC12, and AC20 was greater above cloud base than at cloud base on several cloud passes (especially in flights AC08 and AC20; see Figures 6 and 7 in the supplementary material for these flights). In these flights the estimated r_{ea} values were larger than the measured r_e as a function of D_c and strong updrafts (up to 15 m s^{-1}) were observed above cloud base (see Figures 3b,d and h in the supplementary material). The acceleration of updrafts above the height of cloud base increase supersaturation and thus can induce secondary drop activation. For flights which we observed the increase of N_d with height, high aerosol concentration was observed indicating secondary nucleation of droplets above cloud base. During these flights, cloud profiling was performed up to D_c ~3500 m, and the values of measured r_e were smaller than 13 µm, indicating the suppression of raindrop formation. The analysis of the data from the cloud probe DSDs and CCP-CIP images indicates that indeed no raindrops were present on these flights (not shown). The measurements from AC07 and AC13 over very polluted regions in the Amazon suggest that no raindrops are formed in growing convective clouds under these conditions. Instead, large precipitation particles are formed at cold temperatures in the form of ice. The D_c at which these ice particles are formed depends on the size of the cloud droplets (r_e) at colder temperatures (larger droplets freeze earlier or at lower D_c) [Pruppacher et al., 1998]. This was previously documented by satellite retrievals (Rosenfeld et al., 2011), where glaciation temperatures of convective clouds were strongly dependent on r_e at the -5 °C isotherm, where smaller r_e were correlated with lower glaciation temperatures.

4.2.3 Discussion

The results from cloud probe measurements under clean, polluted, and very polluted conditions highlight the role of aerosol particles in rain and ice formation for growing convective cumulus. Figure 17 summarizes the estimated depths above cloud base at which initiation of rain and ice formation is observed (D_r and D_i), as well as the estimated D_c for rain initiation as indicated from r_{ea} by D_{13}. This figure shows a close relationship between N_a and D_r of $D_r = (5\pm0.7)N_a$, demonstrating the capability to predict the minimum height at which raindrops are expected to form based on cloud base drop concentrations. For flights in which rain was observed (AC19, AC18, and AC09), D_r occurs at heights slightly greater than D_{13}. For cases where neither rain nor ice were observed (AC08, AC12, and AC20), the estimated D_{13} was not reached during the HALO cloud profiling flights. In addition, D_{13} and D_i show similar values for flight AC07,

whereas for flight AC13 the values are less comparable (probably due to an overestimation of N_a, and thus D_{13}, caused by secondary activation above cloud base).

The linear relationship between N_a and D_{13} indicates a regression slope of about 5 m $(cm^{-3})^{-1}$ between D_{13} and the calculated N_a for the Amazon during the dry-to-wet season. This value is slightly larger than the values observed by Freud and Rosenfeld (2012) for other locations around the globe (e.g., India and Israel).

For the flight in cleanest conditions (AC19), the presence of larger aerosol particles (possibly GCCN from sea spray) below cloud base leads to a faster growth of cloud droplets via condensation with height, and consequently r_e is smaller than 13 μm (see Figure 11a) for warm rain initiation. A similar decrease of r_e for rain initiation over ocean was observed by Konwar et al. (2012). While D_r is explained by N_d and well correlated with it, there is no correlation between N_d and D_i.

Figure 18 summarizes the findings for all the vertical profiling flights. It illustrates the vertical development of precipitation water content by symbols representing the amount of DWC and MPWC as a function of D_c and CDP-measured r_e. Also shown are the lines of r_{ea} as a function of D_c. The figure shows that raindrops began to form at r_e of 13 μm for AC09 and AC18. The r_e for rain initiation is slightly smaller (12 μm) on AC19; probably due to the sea spray giant CCN, which accelerate the coalescence for a given r_e. Mixed phase precipitation was initiated on flights AC07 and AC13, well below the height of D_{13} at an r_e of 12 and 10 μm, respectively. Ice starts to form at lower temperatures when the cloud droplets are smaller, as manifested by D_i of -9 and -14 °C for flights AC07 and AC13, respectively. The remaining flights did not reach the height for rain initiation (AC08, AC12, and AC20).

It is evident that raindrops form faster via collision and coalescence process in a cleaner atmosphere. For the polluted cases, raindrops form at colder temperatures (~0 ºC and colder) via collision and coalescence than for clean conditions. Rain can initiate at supercooled temperatures, e,g., -5 °C on AC18. The raindrops were documented to start freezing at -9 °C in AC09. In very polluted conditions, only cloud droplets, but no raindrops were observed at D_c < 4000 m. In these cases, precipitation was initiated as ice particles at D_c > 4000 m. These flights with completely suppressed warm rain were performed over the smoky deforestation arc. Measurements of large updrafts which increase supersaturation within cloud and the higher N_d above cloud base indicate new activation of cloud droplets for flight AC13 (not observed at AC07) in the course of the development of convective cumulus. This secondary activation leads to smaller r_e. For flights where secondary activation was significant, the differences between the estimated r_{ea} and the r_e measurements at same height are larger, because the adiabatic estimation does not consider the secondary activation of droplets above cloud base and thus overestimates the observed size.

5. Conclusions

This study focused on the effects of aerosol particle number concentration on the initiation of rain drops and ice hydrometeors in growing convective cumulus over the Amazon. Data from aerosol and cloud probes on board of the HALO aircraft were used in the analysis. The values of the estimated N_a at cloud base were applied to classify the atmospheric conditions where convective clouds developed as a function of aerosol particle number concentration (i.e., clean, polluted, and very polluted regions). From the estimated N_a, the evolution of r_{ea}, the theoretical r_e assuming adiabatic growth of droplets, with cloud depth above cloud base (D_c) were compared with the observed r_e at the various heights. A DWC value of 0.01 g m^{-3} was used as a threshold for rain initiation or glaciation within clouds. Images from the CCP-CIP probe were used to detect the presence of raindrops and/or ice hydrometeors. The results support the use of r_e ~ 13-14 μm as a threshold for rain initiation in convective clouds. The evolution of the directly observed r_e follows that of the calculated r_{ea} with slight differences as a function of aerosol particle size distributions. Rain initiation

occurred higher in more polluted clouds, as manifested by higher D_c. Rain was initiated at supercooled levels in moderately polluted clouds. In very polluted conditions, warm rain was suppressed completely. This was exacerbated by the occurrence of secondary activation above cloud base, which further reduced r_e compared to r_{ea}. The initiation of ice hydrometeors is also delayed to greater D_c in more polluted clouds, because smaller drops freeze at colder temperatures. Ice was initiated mostly by freezing raindrops in cases when warm rain formation was not completely suppressed. Both the D_{13} and D_r increased linearly with N_a, in agreement with the theoretical considerations of Freud and Rosenfeld (2012). Despite the suspected occasional secondary drop activation, r_e was sufficiently close to r_{ea} to allow a linear relationship in the form of $D_r = (5\pm0.7)N_a$. The observations suggest also that, in the absence of new droplet activation above cloud base, D_{13} is very similar to D_i under very polluted conditions, where raindrops are not formed at warmer temperatures.

These results show that even moderate amounts of smoke, which fill most of the Amazon basin during the drier season, are sufficient to suppress warm rain and elevate its initiation to above the 0 ºC isotherm level. This results in a suppression of rain from small clouds and an invigoration in the deep clouds, as hypothesized by Rosenfeld et al. (2008). While the net effect on rainfall amount is unknown, the redistribution of rain intensities and the resulting vertical latent heating profiles are likely to affect the regional hydrological cycle in ways that need to be studied further.

Acknowledgements

The first two authors of this study were supported by project BACCHUS European Commission FP7-603445. The generous support of the ACRIDICON-CHUVA campaign by the Max Planck Society, the German Aerospace Center (DLR), FAPESP (São Paulo Research Foundation), and the German Science Foundation (Deutsche Forschungsgemeinschaft, DFG) within the DFG Priority Program (SPP 1294) "Atmospheric and Earth System Research with the Research Aircraft HALO (High Altitude and Long Range Research Aircraft)" is greatly appreciated. This study was also supported by EU Project HAIC under FP7-AAT-2012-3.5.1-1. C. Mahnke and R. Weigel received funding by the German Federal Ministry of Education and Research (BMBF, Bundesministerium für Bildung und Forschung) within the joint ROMIC-project SPITFIRE (01LG1205A). In addition, the German Science Foundation within DFG SPP 1294 HALO by contract no VO1504/4-1 and contract no JU 3059/1-1 contribute to support this study. The first author also acknowledges the financial support from the Brazilian funding agencies CAPES and CNPq during his Ph.D. studies.

References

Albrecht, R. I., Morales, C. A. and Silva Dias, M. A. F.: Electrification of precipitating systems over the Amazon: Physical processes of thunderstorm development, J. Geophys. Res., 116(D8), D08209, doi:10.1029/2010JD014756, 2011.

Andreae, M. O.: Correlation between cloud condensation nuclei concentration and aerosol optical thickness in remote and polluted regions, Atmos. Chem. Phys., 9(2), 543–556, doi:10.5194/acp-9-543-2009, 2009.

Andreae, M. O., Rosenfeld, D., Artaxo, P., Costa, A. A., Frank, G. P., Longo, K. M. and Silva-Dias, M. A. F.: Smoking rain clouds over the Amazon., Science, 303(5662), 1337–42, doi:10.1126/science.1092779, 2004.

Andreae, M. O., Artaxo, P., Beck, V., Bela, M., Freitas, S., Gerbig, C., Longo, K., Munger, J. W., Wiedemann, K. T. and

Wofsy, S. C.: Carbon monoxide and related trace gases and aerosols over the Amazon Basin during the wet and dry seasons, Atmos. Chem. Phys., 12(13), 6041–6065, doi:10.5194/acp-12-6041-2012, 2012.

Artaxo, P., Martins, J. V., Yamasoe, M. A., Procópio, A. S., Pauliquevis, T. M., Andreae, M. O., Guyon, P., Gatti, L. V. and Leal, A. M. C.: Physical and chemical properties of aerosols in the wet and dry seasons in Rondônia, Amazonia, J. Geophys. Res. D Atmos., 107(20), 1–14, doi:10.1029/2001JD000666, 2002.

Artaxo, P., Rizzo, L. V, Brito, J. F., Barbosa, H. M. J., Arana, A., Sena, E. T., Cirino, G. G., Bastos, W., Martin, S. T. and Andreae, M. O.: Atmospheric aerosols in Amazonia and land use change: from natural biogenic to biomass burning conditions, Faraday Discuss., 165, 203–235, doi:10.1039/C3FD00052D, 2013.

Baumgardner, D., Brenguier, J. L., Bucholtz, A., Coe, H., DeMott, P., Garrett, T. J., Korolev, A., Krämer, M., Petzold, A., Strapp, W., Pilewskie, P., Taylor, J., Twohy, C., Wendisch, M., Bachalo, W., and Chuang, P. Airborne instruments to measure atmospheric aerosol particles, clouds and radiation: A cook's tour of mature and emerging technology. *Atmospheric Research*, *102*(1), 10-29, 2011.

Beals, M. J., Fugal, J. P., Shaw, R. A., Lu, J., Spuler, S. M. and Stith, J. L.: Holographic measurements of inhomogeneous cloud mixing at the centimeter scale, , 350(6256), 87–90, doi:10.1126/science.aab0751, 2015.

Braga, R. C., Rosenfeld, D., Weigel, R., Jurkat, T., Andreae, M. O., Wendisch, M., Pöhlker, M. L., Klimach, T., Pöschl, U., Pöhlker, C., Voigt, C., Mahnke, C., Borrmann, S., Albrecht, R. I., Molleker, S., Vila, D. A., Machado, L. A. T., and Artaxo, P.: Comparing calculated microphysical properties of tropical convective clouds at cloud base with measurements during the ACRIDICON-CHUVA campaign, Atmos. Chem. Phys. Discuss., doi:10.5194/acp-2016-872, in review, 2016.

Brenguier, J. L., Bachalo, W. D., Chuang, P. Y., Esposito, B. M., Fugal, J., Garrett, T., Gayet, J. F., Gerber, H., Heymsfield, A., Kokhanovsky, A., Korolev, A., Lawson, R. P., Rogers, D. C., Shaw, R. A., Strapp, W. and Wendisch, M.: In Situ Measurements of Cloud and Precipitation Particles, in Airborne Measurements for Environmental Research: Methods and Instruments, pp. 225–301., 2013.

Burnet, F. and Brenguier, J.L.: Observational Study of the Entrainment-Mixing Process in Warm Convective Clouds, J. Atmos. Sci., 64(6), 1995–2011, doi:10.1175/JAS3928.1, 2007.

Chen, R., R. Wood, Z. Li, R. Ferraro, and F. Chang: Studying the vertical variation of cloud droplet effective radius using ship and spaceborne remote sensing data, J. Geophys. Res., 113, D00A02, doi:10.1029/2007JD009596, 2008.

Fan, J., Leung, L. R., Demott, P. J., Comstock, J. M., Singh, B., Rosenfeld, D., Tomlinson, J. M., White, A., Prather, K. A., Minnis, P., Ayers, J. K. and Min, Q.: Aerosol impacts on California winter clouds and precipitation during calwater 2011: Local pollution versus long-range transported dust, Atmos. Chem. Phys., 14(1), 81–101, doi:10.5194acp-14-81-2014f, 2014.

Freud, E. and Rosenfeld, D.: Linear relation between convective cloud drop number concentration and depth for rain

initiation, J. Geophys. Res. Atmos., 117(2), 1–13, doi:10.1029/2011JD016457, 2012.

Freud, E., Rosenfeld, D. and Kulkarni, J. R.: Resolving both entrainment-mixing and number of activated CCN in deep convective clouds, Atmos. Chem. Phys., 11(24), 12887–12900, doi:10.5194/acp-11-12887-2011, 2011.

Frey, W., Borrmann, S., Kunkel, D., Weigel, R., De Reus, M., Schlager, H., Roiger, A., Voigt, C., Hoor, P., Curtius, J., Krämer, M., Schiller, C., Volk, C. M., Homan, C. D., Fierli, F., Di Donfrancesco, G., Ulanovsky, A., Ravegnani, F., Sitnikov, N. M., Viciani, S., D'Amato, F., Shur, G. N., Belyaev, G. V., Law, K. S. and Cairo, F.: In situ measurements of tropical cloud properties in the West African Monsoon: Upper tropospheric ice clouds, mesoscale convective system outflow, and subvisual cirrus, Atmos. Chem. Phys., 11(12), 5569–5590, doi:10.5194/acp-11-5569-2011, 2011.

Gerber, H.: Microphysics of marine stratocumulus clouds with two drizzle modes, J. Atmos. Sci., 53(12), 1649–1662, 1996.

Khain, A., Rosenfeld, D. and Pokrovsky, A.: Aerosol impact on the dynamics and microphysics of deep convective clouds, Q. J. R. Meteorol. Soc., 131, 2639–2663 ST – Aerosol impact on the dynamics and, doi:10.1256/qj.04.62, 2005.

Khain, A., Ovtchinnikov, M., Pinsky, M., Pokrovsky, A. and Krugliak, H.: Notes on the state-of-the-art numerical modeling of cloud microphysics, Atmos. Res., 55(3-4), 159–224, doi:10.1016/S0169-8095(00)00064-8, 2000.

Klein, S. A., McCoy, R. B., Morrison, H., Ackerman, A. S., Avramov, A., Boer, G. De, Chen, M., Cole, J. N. S., Del Genio, A. D., Falk, M., Foster, M. J., Fridlind, A., Golaz, J.C., Hashino, T., Harrington, J. Y., Hoose, C., Khairoutdinov,

Konwar, M., Maheskumar, R. S., Kulkarni, J. R., Freud, E., Goswami, B. N. and Rosenfeld, D.: Aerosol control on depth of warm rain in convective clouds, J. Geophys. Res. Atmos., 117(13), 1–10, doi:10.1029/2012JD017585,2012, 2012.

Kuhn, U., Ganzeveld, L., Thielmann, A., Dindorf, T., Schebeske, G., Welling, M., Sciare, J., Roberts, G., Meixner, F. X., Kesselmeier, J., Lelieveld, J., Kolle, O., Ciccioli, P., Lloyd, J., Trentmann, J., Artaxo, P. and Andreae, M. O.: Impact of Manaus City on the Amazon Green Ocean atmosphere: ozone production, precursor sensitivity and aerosol load, Atmos. Chem. Phys., 10(19), 9251–9282, doi:10.5194/acp-10-9251-2010, 2010.

Lance, S.: Coincidence errors in a cloud droplet probe (CDP) and a cloud and aerosol spectrometer (CAS), and the improved performance of a modified CDP, J. Atmos. Ocean. Technol., 29(10), 1532–1541, doi:10.1175/JTECH-D-11-00208.1, 2012.

Lance, S., Brock, C. A., Rogers, D. and Gordon, J. A.: Water droplet calibration of the Cloud Droplet Probe (CDP) and in-flight performance in liquid, ice and mixed-phase clouds during ARCPAC, Atmos. Meas. Tech., 3(6), 1683–1706, doi:10.5194/amt-3-1683-2010, 2010.

M. F., Larson, V. E., Liu, X., Luo, Y., McFarquhar, G. M., Menon, S., Neggers, R. A. J., Park, S., Poellot, M. R.,

Schmidt, J. M., Sednev, I., Shipway, B. J., Shupe, M. D., Spangenberg, D. A., Sud, Y. C., Turner, D. D., Veron, D. E., Salzen, K. Von, Walker, G. K., Wang, Z., Wolf, A. B., Xie, S., Xu, K.-M., Yang, F. and Zhang, G.: Intercomparison of model simulations of mixed-phase clouds observed during the ARM Mixed-Phase Arctic Cloud Experiment. I: single-layer cloud, Q. J. R. Meteorol. Soc., 135(641), 979–1002, doi:10.1002/qj.416, 2009.

Lee, G. W., Seed, A. W. and Zawadzki, I.: Modeling the variability of drop size distributions in space and time, J. Appl. Meteorol. Climatol., 46(6), 742–756, doi:10.1175/JAM2505.1, 2007.

Li, Z., Li, C., Chen, H., Tsay, S. C., Holben, B., Huang, J., Li, B., Maring, H., Qian, Y., Shi, G., Xia, X., Yin, Y., Zheng, Y. and Zhuang, G.: East Asian Studies of Tropospheric Aerosols and their Impact on Regional Climate (EAST-AIRC): An overview, J. Geophys. Res. Atmos., 116(4), doi:10.1029/2010JD015257, 2011.

Liu, P. S. K., Leaitch, W. R., Strapp, J. W., and Wasey, M. A., Response of Particle Measuring Systems airborne ASASP and PCASP to NaCl and latex particles: Aerosol Sci. Tech., 16, 83-95, 1992.

Machado L, Silva Dias M, Morales C, Fisch G, Vila D, Albrecht R, Goodman S, Calheiros A, Biscaro T, Kummerow C, Cohen J, Fitzjarrald D, Nascimento E, Sakamoto M, Cunningham C, Chaboureau J, Petersen W, Adams D, Baldini L, Angelis C, Sapucci L, Salio P, Barbosa H, Landulfo E, Souza R, Blakeslee R, Bailey J, Freitas S, Lima W, Tokay A , The Chuva Project: How Does Convection Vary across Brazil?, Bull. Am. Meteorol. Soc., doi: 10.1175/BAMS-D-13-00084.1, 2014.

Mallaun, C., Giez, A. and Baumann, R.: Calibration of 3-D wind measurements on a single-engine research aircraft, Atmos. Meas. Tech., 8(8), 3177–3196, doi:10.5194/amt-8-3177-2015, 2015.

Martin, S. T., Artaxo, P., Machado, L. A. T., Manzi, A. O., Souza, R. A. F., Schumacher, C., Wang, J., Andreae, M. O., Barbosa, H. M. J., Fan, J., Fisch, G., Goldstein, A. H., Guenther, A., Jimenez, J. L., Pöschl, U., Silva Dias, M. A., Smith, J. N. and Wendisch, M.: Introduction: Observations and Modeling of the Green Ocean Amazon (GoAmazon2014/5), Atmos. Chem. Phys., 16(8), 4785–4797, doi:10.5194/acp-16-4785-2016, 2016.

Paluch, I. R. (1979). The entrainment mechanism in Colorado cumili. J. Atmos. Sci., 36:2467–2478

Pinsky, M. B. and Khain, A.: Effects of in-cloud nucleation and turbulence on droplet spectrum formation in cumulus clouds, Q. J. R. Meteorol. Soc., 128(580), 501–533, doi:10.1256/003590002321042072, 2002.

Pöhlker, M. L., Pöhlker, C., Klimach, T., Angelis, I. H. de, Barbosa, H. M. J., Brito, J., Samara Carbone, Cheng, Y., Chi, X., Ditas, F., Ditz, R., Gunthe, S. S., Kesselmeier, J., Könemann, T., Lavrič, J. V., Martin, S. T., Moran-Zuloaga, D., Rose, D., Saturno, J., Su, H., Thalman, R., Walter, D., Wang, J., Wolff, S., Artaxo, P., Andreae, M. O. and Pöschl, U.: Long-term observations of atmospheric aerosol , cloud condensation nuclei concentration and hygroscopicity in the Amazon rain forest – Part 1 : Size-resolved characterization and new model parameterizations for CCN prediction, Atmos. Chem. Phys., (July), doi:10.5194/acp-2016-519, 2016.

Pöschl, U., Martin, S. T., Sinha, B., Chen, Q., Gunthe, S. S., Huffman, J. A., Borrmann, S., Farmer, D. K., Garland, R.

M., Helas, G., Jimenez, J. L., King, S. M., Manzi, A., Mikhailov, E., Pauliquevis, P., Petters, M. D., Prenni, A. J., Roldin, P., Rose, D., Schneider, J., Su, H., Zorn, S. R., Artaxo, P. and Andreae, M. O.: Rainforest Aerosols as Biogenic Nuclei of Clouds and Precipitation in the Amazon, Science (80-.)., 329(2010), 1513–1516, doi:10.1126/science.1191056, 2010.

Prabha, T. V., A. Khain, R. S. Maheshkumar, G. Pandithurai, J. R. Kulkarni, M. Konwar, and B. N. Goswami: Micro-physics of premonsoon and monsoon clouds as seen from i n situ measurements during the Cloud Aerosol Interaction and Precipitation Enhancement Experiment (CAIPEEX), J. Atmos. Sci., 68, 1882– 1901, 2011.
Pruppacher, H. R., Klett, J. D. and Wang, P. K.: Microphysics of Clouds and Precipitation, Aerosol Sci. Technol., 28, 381–382, doi:10.1080/02786829808965531, 1998.

Ramanathan, V., Crutzen, P. J., Lelieveld, J., Mitra, A. P., Althausen, D., Anderson, J., Andreae, M. O., Cantrell, W., Cass, G. R., Chung, C. E., Clarke, A. D., Coakley, J. A., Collins, W. D., Conant, W. C., Dulac, F., Heintzenberg, J., Heymsfield, A. J., Holben, B., Howell, S., Hudson, J., Jayaraman, A., Kiehl, J. T., Krishnamurti, T. N., Lubin, D., McFarquhar, G., Novakov, T., Ogren, J. A., Podgorny, I. A., Prather, K., Priestley, K., Prospero, J. M., Quinn, P. K., Rajeev, K., Rasch, P., Rupert, S., Sadourny, R., Satheesh, S. K., Shaw, G. E., Sheridan, P. and Valero, F. P. J.: Indian Ocean Experiment: An integrated analysis of the climate forcing and effects of the great Indo-Asian haze, J. Geophys. Res., 106(D22), 28371, doi:10.1029/2001JD900133, 2001.

Rosenfeld, D.: Suppression of Rain and Snow by Urban and Industrial Air Pollution, Science (80-.)., 287, 1793–1796, doi:10.1126/science.287.5459.1793, 2000.

Rosenfeld, D. and Gutman, G.: Retrieving microphysical properties near the tops of potential rain clouds by multispectral analysis of AVHRR data, Atmos. Res., 34(1-4), 259–283, doi:10.1016/0169-8095(94)90096-5, 1994.

Rosenfeld, D. and Lensky, I. M.: Satellite-Based Insights into Precipitation Formation Processes in Continental and Maritime Convective Clouds, Bull. Am. Meteorol. Soc., 79(11), 2457–2476, doi:10.1175/1520-0477, 1998.

Rosenfeld, D. and Woodley, W. L. W.: Deep convective clouds with sustained supercooled liquid water down to -37.5 degrees C, Nature, 405(6785), 440–2, 2000.

Rosenfeld, D., Lohmann, U., Raga, G. B., O'Dowd, C. D., Kulmala, M., Fuzzi, S., Reissell, A. and Andreae, M. O.: Flood or drought: how do aerosols affect precipitation?, Science, 321(5894), 1309–13, doi:10.1126/science.1160606, 2008.

Rosenfeld, D., Yu, X., Liu, G., Xu, X., Zhu, Y., Yue, Z., Dai, J., Dong, Z., Dong, Y. and Peng, Y.: Glaciation temperatures of convective clouds ingesting desert dust, air pollution and smoke from forest fires, Geophys. Res. Lett., 38(21), 2006–2010, doi:10.1029/2011GL049423, 2011.

Rosenfeld, D., Wang, H. and Rasch, P. J.: The roles of cloud drop effective radius and LWP in determining rain properties in marine stratocumulus, Geophys. Res. Lett., 39(13), 1–6, doi:10.1029/2012GL052028, 2012a.

Rosenfeld, D., Williams, E., Andreae, M. O., Freud, E., Pöschl, U. and Rennó, N. O.: The scientific basis for a satellite mission to retrieve CCN concentrations and their impacts on convective clouds, Atmos. Meas. Tech., 5(8), 2039–2055, doi:10.5194/amt-5-2039-2012, 2012b.

Rosenfeld, D., Andreae, M. O., Asmi, A., Chin, M., De Leeuw, G., Donovan, D. P., Kahn, R., Kinne, S., Kiveks, N., Kulmala, M., Lau, W., Schmidt, K. S., Suni, T., Wagner, T., Wild, M. and Quaas, J.: Global observations of aerosol-cloud-precipitation-climate interactions, Rev. Geophys., 52(4), 750–808, doi:10.1002/2013RG000441, 2014a.

Rosenfeld, D., Liu, G., Yu, X., Zhu, Y., Dai, J., Xu, X. and Yue, Z.: High-resolution (375 m) cloud microstructure as seen from the NPP/VIIRS satellite imager, Atmos. Chem. Phys., 14(5), 2479–2496, doi:10.5194/acp-14-2479-2014, 2014b.

Segal, Y., Pinsky, M. and Khain, A.: The role of competition effect in the raindrop formation, Atmos. Res., 83(1), 106–118, doi:10.1016/j.atmosres.2006.03.007, 2007.

Tao, W., Chen, J. and Li, Z.: Impact of aerosols on convective clouds and precipitation, Rev. Geophys.,50, RG2001, doi:10.1029/2011RG000369, 2012.

Twomey, S.: The nuclei of natural cloud formation part II: The supersaturation in natural clouds and the variation of cloud droplet concentration, Geofis. Pura e Appl., 43(1), 243–249, doi:10.1007/BF01993560, 1959.

VanZanten, M., B. Stevens, G. Vali, and D. Lenschow: Observations of drizzle in nocturnal marine stratocumulus, J. Atmos. Sci., 62(1), 88–106, 2005

Voigt, C., Schumann, U., Jurkat, T., Schäuble, D., Schlager, H., Petzold, A., Gayet, J. F., Krämer, M., Schneider, J., Borrmann, S., Schmale, J., Jessberger, P., Hamburger, T., Lichtenstern, M., Scheibe, M., Gourbeyre, C., Meyer, J., Kübbeler, M., Frey, W., Kalesse, H., Butler, T., Lawrence, M. G., Holzäpfel, F., Arnold, F., Wendisch, M., Döpelheuer, A., Gottschaldt, K., Baumann, R., Zöger, M., Sölch, I., Rautenhaus, M. and Dörnbrack, A.: In-situ observations of young contrails–overview and selected results from the CONCERT campaign. *Atmospheric Chemistry and Physics*, *10*(18), 9039-9056, 2010.

Voigt, C., Schumann, U., Jessberger, P., Jurkat, T., Petzold, A., Gayet, J. F., Krmer, M., Thornberry, T. and Fahey, D. W.: Extinction and optical depth of contrails, Geophys. Res. Lett., 38(11), doi:10.1029/2011GL047189, 2011.

Voigt, C., Schumann, U., Minikin, A., Abdelmonem, A., Afchine, A., Borrmann, S., Boettcher, M., Buchholz, B., Bugliaro, L., Costa, A., Curtius, J., Dollner, M., Dörnbrack, A., Dreiling, V., Ebert, V., Ehrlich, A., Fix, A., Forster, L., Frank, F., Fütterer, D., Giez, A., Graf, K., Grooß, J., Groß, S., Heimerl, K., Heinold, B., Hüneke, T., Järvinen, E., Jurkat, T., Kaufmann, S., Kenntner, M., Klingebiel, M., Klimach, T., Kohl, R., Krämer, M., Krisna, T., Luebke, A., Mayer, B., Mertes, S., Molleker, S., Petzold, A., Pfeilsticker, K., Port, M., Rapp, M., Reutter, P., Rolf, C., Rose, D., Sauer, D., Schäfler, A., Schlage, R., Schnaiter, M., Schneider, J., Spelten, N., Spichtinger, P., Stock, P., Walser, A., Weigel, R., Weinzierl, B., Wendisch, M., Werner, F., Wernli, H., Wirth, M., Zahn, A., Ziereis, H. and Zöger, M.: ML-CIRRUS - The

airborne experiment on natural cirrus and contrail cirrus with the high-altitude long-range research aircraft HALO, Bull. Am. Meteorol. Soc., doi:10.1175/BAMS-D-15-00213.1, 2017.

Wendisch, M., Pöschl, U., Andreae, M. O., Machado, L. A. T., Albrecht, R., Schlager, H., Rosenfeld, D., Martin, S. T., Abdelmonem, A., Afchine, A., Araùjo, A., Artaxo, P., Aufmhoff, H., Barbosa, H. M. J., Borrmann, S., Braga, R., Buchholz, B., Cecchini, M. A., Costa, A., Curtius, J., Dollner, M., Dorf, M., Dreiling, V., Ebert, V., Ehrlich, A., Ewald, F., Fisch, G., Fix, A., Frank, F., Fütterer, D., Heckl, C., Heidelberg, F., Hüneke, T., Jäkel, E., Järvinen, E., Jurkat, T., Kanter, S., Kästner, U., Kenntner, M., Kesselmeier, J., Klimach, T., Knecht, M., Kohl, R., Kölling, T., Krämer, M., Krüger, M., Krisna, T. C., Lavric, J. V., Longo, K., Mahnke, C., Manzi, A. O., Mayer, B., Mertes, S., Minikin, A., Molleker, S., Münch, S., Nillius, B., Pfeilsticker, K., Pöhlker, C., Roiger, A., Rose, D., Rosenow, D., Sauer, D., Schnaiter, M., Schneider, J., Schulz, C., de Souza, R. A. F., Spanu, A., Stock, P., Vila, D., Voigt, C., Walser, A., Walter, D., Weigel, R., Weinzierl, B., Werner, F., Yamasoe, M. A., Ziereis, H., Zinner, T. and Zöger, M.: The ACRIDICON-CHUVA campaign: Studying tropical deep convective clouds and precipitation over Amazonia using the new German research aircraft HALO, Bull. Am. Meteorol. Soc., 160128144638003, doi:10.1175/BAMS-D-14-00255.1, 2016.

Williams, E.: Contrasting convective regimes over the Amazon: Implications for cloud electrification, J. Geophys. Res., 107(D20), 1–19, doi:10.1029/2001JD000380, 2002.

Figure captions

Figure 1 a) HALO flight tracks during the ACRIDICON-CHUVA experiment. The flight number is indicated at the bottom by colors; b) Flight patterns below and in convective clouds during the ACRIDICON-CHUVA campaign.

Figure 2 a) Precipitation probability as a function of r_e for the CCP-CDP probe for different DWC thresholds (black – DWC > 0.01 g m^{-3}; blue – DWC > 0.02 g m^{-3}; green – DWC > 0.03 g m^{-3}; gold – DWC > 0.05 g m^{-3}; red – DWC > 0.1 g m^{-3}). The dashed line indicates the number of cases (in seconds for each 1-s cloud pass) for each r_e size interval (right axis); b) Similar for the CAS-DPOL probe.

Figure 3 Cloud droplet effective radius (r_e) calculated from the CCP-CDP data versus r_e calculated from the CAS-DPOL data for all flights shown in Figure 1a.

Figure 4 a) Droplet mean volume radius versus cloud droplet effective radius (r_e) for 1-Hz averaged droplet size distributions from CCP-CDP measured during various flights over the Amazon; b) similar for CAS-DPOL. The color-coding denotes different flights over the Amazon. The number of measurements that were used to calculate the linear best fit for each location is denoted by "n" in the legend. The r_e and r_v mean linear relationship for all flights is shown below the linear relationship for each flight in black color.

Figure 5 Cloud droplet concentration measured with CCP-CDP as a function of temperature for flight AC07. Each dot indicates a 1-Hz average concentration. The sample number (N) and the approximate start time of the cloud profile are shown at the top of the panel.

Figure 6 a) Mean cloud droplet size distribution calculated from the CCP-CDP data for a cloud pass at cloud base during flight AC07. The flight number, initial time of cloud pass, and duration in seconds are shown at the top of graph. The mean total number of droplets (N_{dmean}), the maximum total number of droplets (N_{dmax}) in one second for this cloud pass, and the approximate height (H) and temperature (T) are shown at the upper-right corner of the graph; b) Cloud droplet effective radius (r_e) calculated from CCP-CDP as a function of temperature indicated with dots. The black line indicates the estimated adiabatic effective radius (r_{ea}) as a function of temperature.

Figure 7a-c. Droplet size distribution composite from the CCP-CDP and CCP-CIP probes (left panel). Similar for indicated cloud water content (CWC) in the right panel. Indicated at the top of the panels are the HALO flight number, date, time of flight (UTC), duration of cloud pass in seconds, temperature (T) and altitude (H) above sea level, and the mean values for the total number of droplets (N_d), CWC, DWC, RWC, and r_e. The color bars indicate the height of HALO during the cloud pass. On the right side of the panels CCP-CIP images corresponding to the cloud pass are shown.

Figure 8 Image taken from the HALO cockpit just before the aircraft penetration of a convective cloud with lightning activity during flight AC07. In this case, the cloud pass height was 9,022 m (temperature ~ -25 ºC) and the maximum CWC measured was 0.55 g m^{-3}.

Figure 9 a) Cloud droplet effective radius (r_e) as a function of cloud depth (D_c) for flight AC07. The line indicates the r_e estimated for adiabatic growth (r_{ea}) from cloud base (dashed lines indicate the r_{ea} values considering the uncertainty of the estimate). The height of 0 ºC is indicated by a black horizontal bar across the r_{ea} line. The estimated adiabatic number of droplets (N_a) at cloud base is shown at the top of the figure. b) Similar to a) for Cloud water content (adiabatic values are shown by lines).

Figure 10 a) Cloud droplet concentrations measured with the CCP-CDP as a function of temperature for flight AC19. Each dot indicates 1Hz average concentration. The sample number in seconds (N) and the start time of the cloud profile are shown at the top of the panel; b) Similar to Figure 9 for flight AC19.
Figures 11 a-b) Similar to Figures 7a-c for flight AC19.

Figure 12 Aerosol size distribution below cloud base calculated from the PCASP probe for typical clean, polluted, and very polluted regions (mean - dashed line, cumulative - continuous line) for flights AC12 (very polluted), AC18 (polluted), and AC19 (clean). The flight numbers are indicated by colors at the top of the panel.

Figure 13 a) Cloud droplet concentrations measured with the CCP-CDP as a function of temperature for flight AC09. Each dot indicates 1-Hz average concentration. The sample number in seconds (N) and the start time of the cloud profile are shown at the top of the panel; b) Similar to Figure 9 for flight AC09.

Figures 14 a-b) Similar to Figures 7a-c for flight AC09.

Figure 15 a) Cloud droplet concentration measured with the CCP-CDP probe as a function of temperature for flight AC13. Each dot indicates a 1-Hz average concentration. The sample number and the approximate time of the cloud profile are shown at the top of the panel; b) Similar to figure 9 for Flight AC13.

Figures 16 Similar to Figures 7a-c for flight AC13.

Figure 17. Cloud depth (D_c) as a function of the estimated adiabatic number of droplets (N_a) at cloud base. D_c for adiabatic cloud droplet effective radius (r_{ea}) equal 13 μm (or D_{13}) are indicated by triangles. Similar for cloud depth of rain initiation (D_r) [indicated by circles] and cloud depth for ice initiation (D_i) [indicated by asterisk]. The flight numbers are indicated by colors on the right side of the panel. The values of D_{13}, D_r, and D_i are shown in Table 1. The black line indicates the linear equation for D_{13} as a function of N_a for all flights, where: $D_{13} = (5 \pm 0.7) \cdot N_a$.

Figure 18 CDP-measured cloud droplet effective radius (r_e) (colored dots) and estimated cloud droplet adiabatic effective radius (r_{ea}) (colored lines) as a function of cloud depth (D_c) for all flights (indicated by colors). The height of 0 ºC is indicated by a horizontal bar across the r_{ea} line. The circles indicate the approximate values of drizzle water content (DWC) calculated from the CCP-CIP data, the range of DWC values is indicated in the table at the upper-right side of the figure. The star symbols indicate approximate mixed phase drizzle water content (MPWC) values calculated from the CCP-CIP data (indicated in the table at the bottom-right side of the figure). The temperature in ºC of rain or ice initiation (D_r and D_i, respectively) is indicated by colored numbers close to the circle or star symbols.

Table captions

Table 1. List of abbreviations and symbols.

Table 2. Description of cloud probes, size range intervals and hydrometeor shapes observed on CCP-CIP images used to calculate CWC, DWC, RWC and MPWC.

Table 3. Classification of each flight as a function of N_a at cloud base. The values of cloud base height (*Cbh*) and temperature (T), D_{13}, D_r and D_i in m and temperatures in ºC are also shown for convective cloud measurements of each flight.

Tables

Table 1. List of abbreviations and symbols.

Abbreviation/notation	Description	Units
ACRIDICON-CHUVA	Aerosol, Cloud, Precipitation, and Radiation Interactions and Dynamics of Convective Cloud Systems - CHUVA (Cloud processes of tHe main precipitation systems in Brazil: A contribUtion to cloud resolVing modeling and to the GPM [Global Precipitation Measurements])	-
CAS-DPOL	Cloud and Aerosol Spectrometer	-
Cbh	Cloud base height	m
CCP-CDP	Cloud Combination Probe - Cloud Droplet Probe	-
CCP-CIP	Cloud Combination Probe - Cloud Imaging Probe	-
CCN	Cloud Condensation Nuclei	cm^{-3}
CWC	Cloud water content	$g\ m^{-3}$
CWC_a	Adiabatic cloud water content	$g\ m^{-3}$
D_c	Cloud depth - distance from cloud base	m
D_r	Cloud depth where first drizzle with drop shape was detected	m
D_i	Cloud depth where first drizzle with ice shape was detected	m
DWC	Drizzle Water Content	$g\ m^{-3}$
DSD	Cloud-droplet size distribution	$cm^{-3}\ \mu m^{-1}$
D_{13}	Cloud depth where r_{ea} = 13 μm	m
IN	Ice Nuclei	cm^{-3}
K	The collection kernel of a pair of droplets	$cm^{-3}\ s^{-1}$
MPWC	Mixed Phase Water Content	$g\ m^{-3}$
M_v	Mean volume cloud droplet	μm^{-3}
M_{va}	Adiabatic mean volume cloud droplet	μm^{-3}
N_d	Number concentration of droplets	cm^{-3}
N_a	Adiabatic number concentration of droplets	cm^{-3}
PCASP	Passive Cavity Aerosol Spectrometer Probe	-
PSD	Aerosol particle size distribution	$cm^{-3}\ \mu m^{-1}$
r_e	The effective radius of the cloud droplet spectra	μm
r_{ea}	The adiabatic effective radius of the cloud droplet spectra	μm
r_v	The mean volume radius of the cloud droplets	μm
RWC	Rainwater Content	$g\ m^{-3}$
S	Supersaturation	%
T	Temperature	ºC
W	Vertical velocity	$m\ s^{-1}$

Table 2. Description of cloud probes, size range intervals and hydrometeor shapes observed on CCP-CIP images used to calculate CWC, DWC, RWC and MPWC.

Abbreviation/Notation	Instrument	Size range	Hydrometeor shapes
CWC	CCP-CDP/CAS-DPOL	3-50 μm	Cloud droplets
DWC	CCP-CIP	75-250 μm	Cloud droplets and raindrops
RWC	CCP-CIP	250-960 μm	Cloud droplets and raindrops
MPWC	CCP-CIP	75-960 μm	Cloud droplets and ice particles

Table 3. Classification of each flight as a function of N_a at cloud base. The values of cloud base height (*Cbh*) and temperature (*T*), D_{13}, D_r and D_i in m and temperatures in ºC are also shown for convective cloud measurements of each flight.

Flight	*Cbh* (m)/ *T* (ºC)	N_a (cm^{-3})	D_{13} (m)	D_r (m)	*T*(ºC)	D_i (m)	*T*(ºC)	Classification
AC07	1900 / 16	963	4500	-	-	4537	-9.1	very polluted
AC08	1100 / 20	920	3900	-	-	-	-	very polluted
AC09	1200 / 19.5	566	2400	3000	2.4	5217	-9.2	polluted
AC12	2200 / 15.5	1546	9000	-	-	-	-	very polluted
AC13	2200 / 15.5	1080	5500	-	-	4800	-14.1	very polluted
AC18	1700 / 17	666	2900	3800	-5.7	-	-	polluted
AC19	600 / 22	276	1000	1660	10	-	-	clean
AC20	1900 / 16.5	987	5000	-	-	-	-	very polluted

Figures

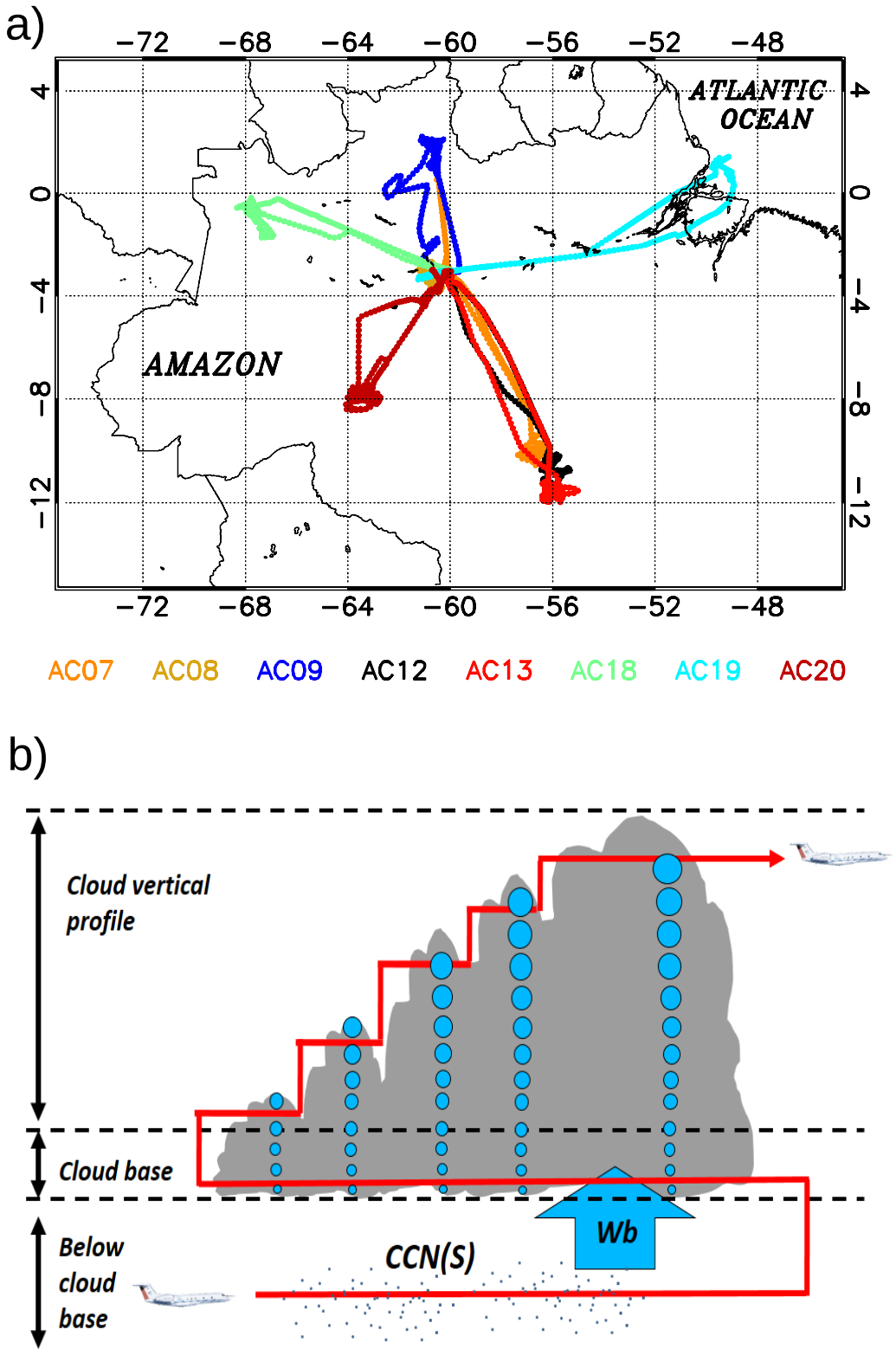

865

Figure 1 a) HALO flight tracks during the ACRIDICON-CHUVA experiment. The flight number is indicated at the bottom by colors; b) Flight patterns below and in convective clouds during the ACRIDICON-CHUVA campaign.

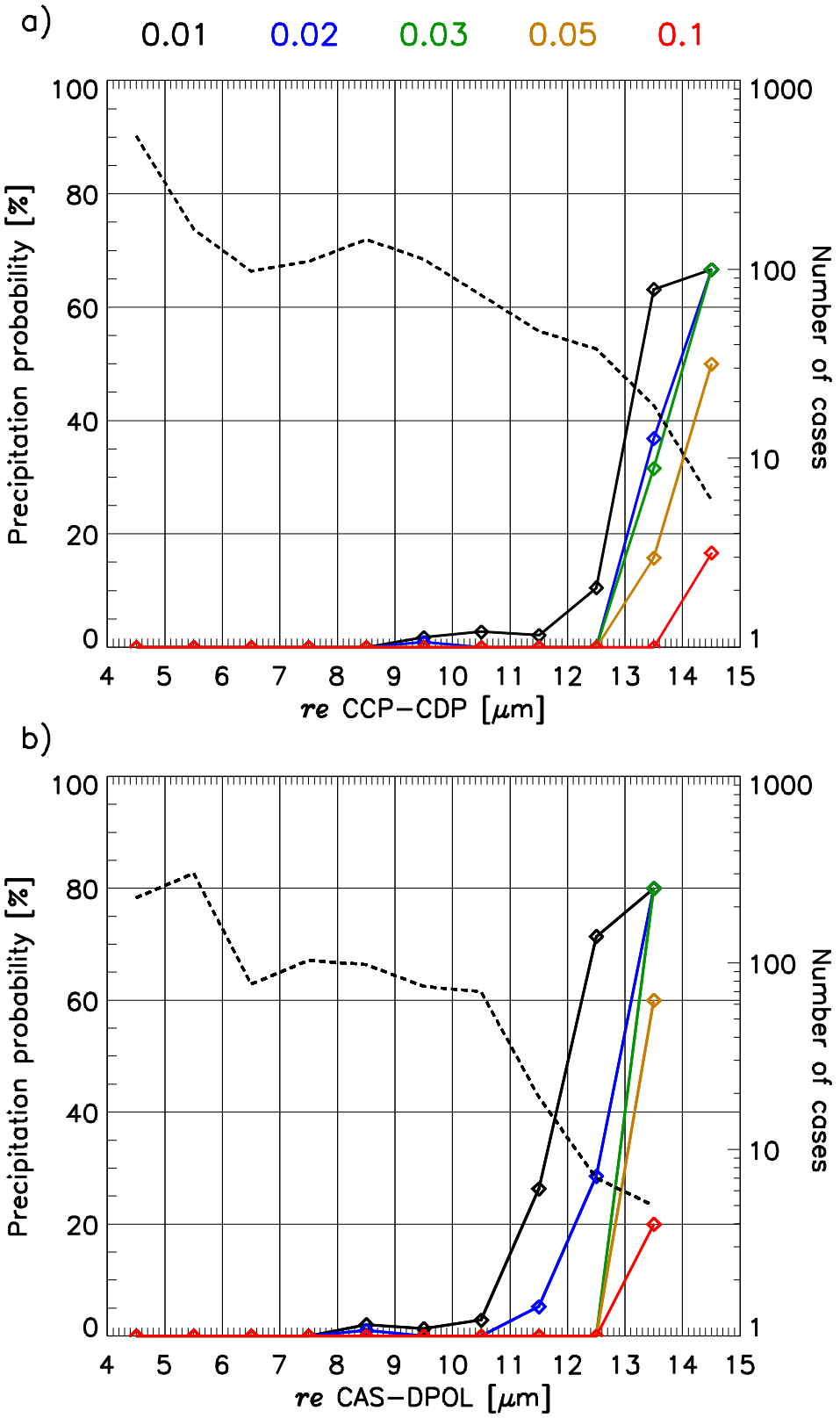

870 **Figure 2 a) Precipitation probability as a function of r_e for the CCP-CDP probe for different DWC thresholds (black – DWC > 0.01 g m^{-3}; blue – DWC > 0.02 g m^{-3}; green – DWC > 0.03 g m^{-3}; gold – DWC > 0.05 g m^{-3}; red – DWC > 0.1 g m^{-3}). The dashed line indicates the number of cases (in seconds for each 1-s cloud pass) for each r_e size interval (right axis); b) Similar for the CAS-DPOL probe.**

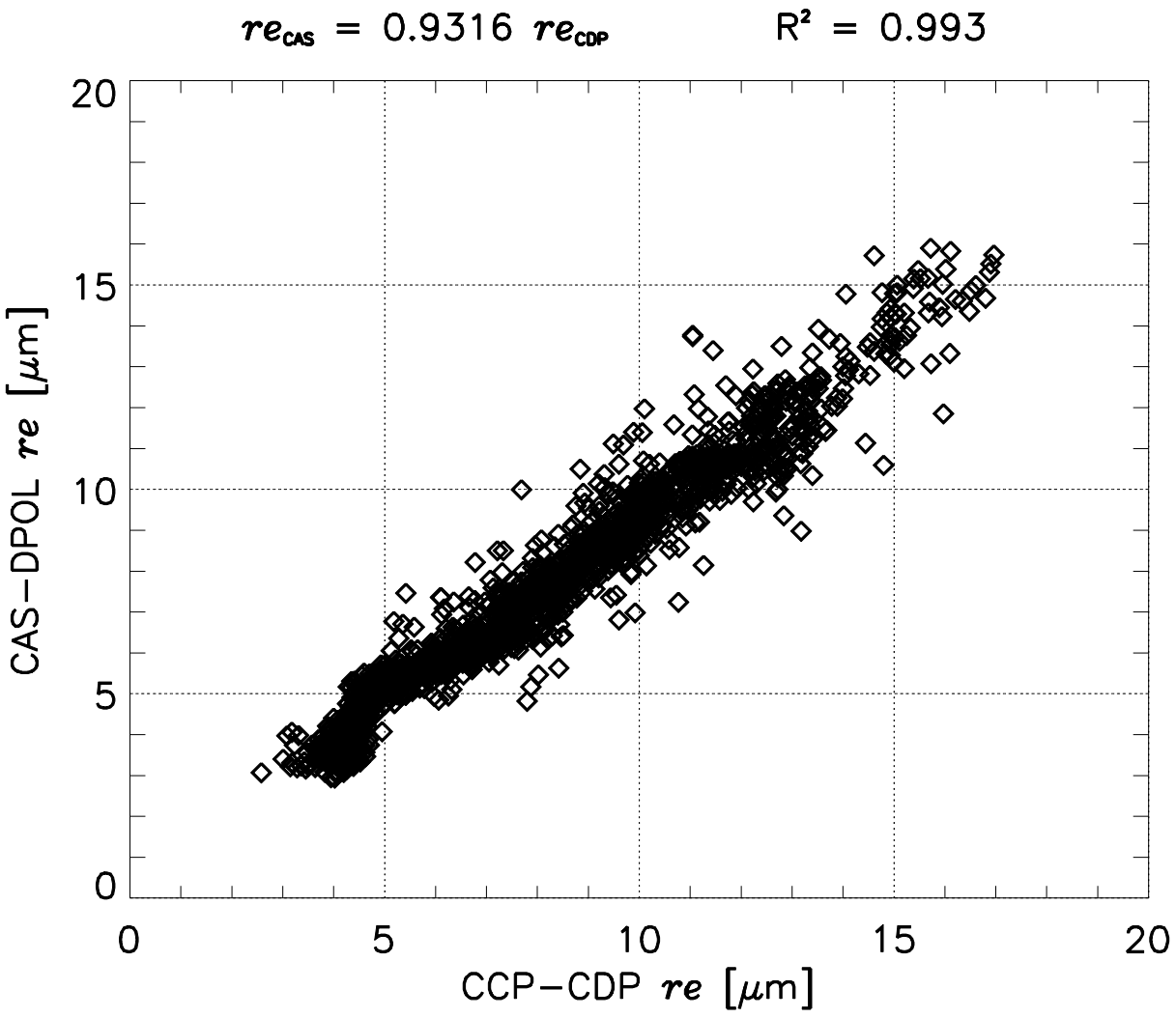

875

Figure 3 Cloud droplet effective radius (r_e) calculated from the CCP-CDP data versus r_e calculated from the CAS-DPOL data for all flights shown in Figure 1a.

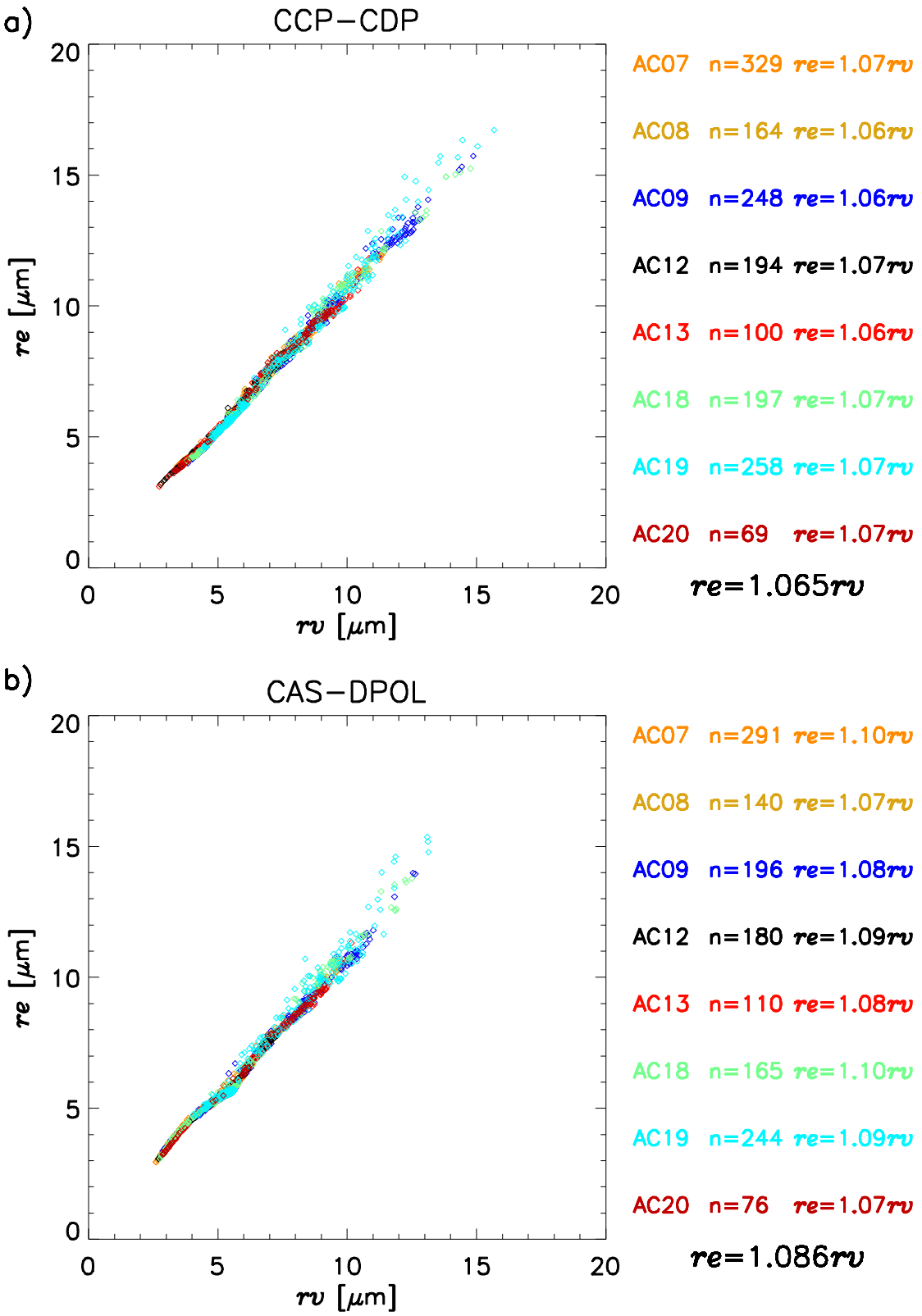

Figure 4 a) Droplet mean volume radius versus cloud droplet effective radius (r_e) for 1-Hz averaged droplet size distributions from CCP-CDP measured during various flights over the Amazon; b) similar for CAS-DPOL. The color-coding denotes different flights over the Amazon. The number of measurements that were used to calculate the linear best fit for each location is denoted by "n" in the legend. The r_e and r_v mean linear relationship for all flights is shown below the linear relationship for each flight in black color.

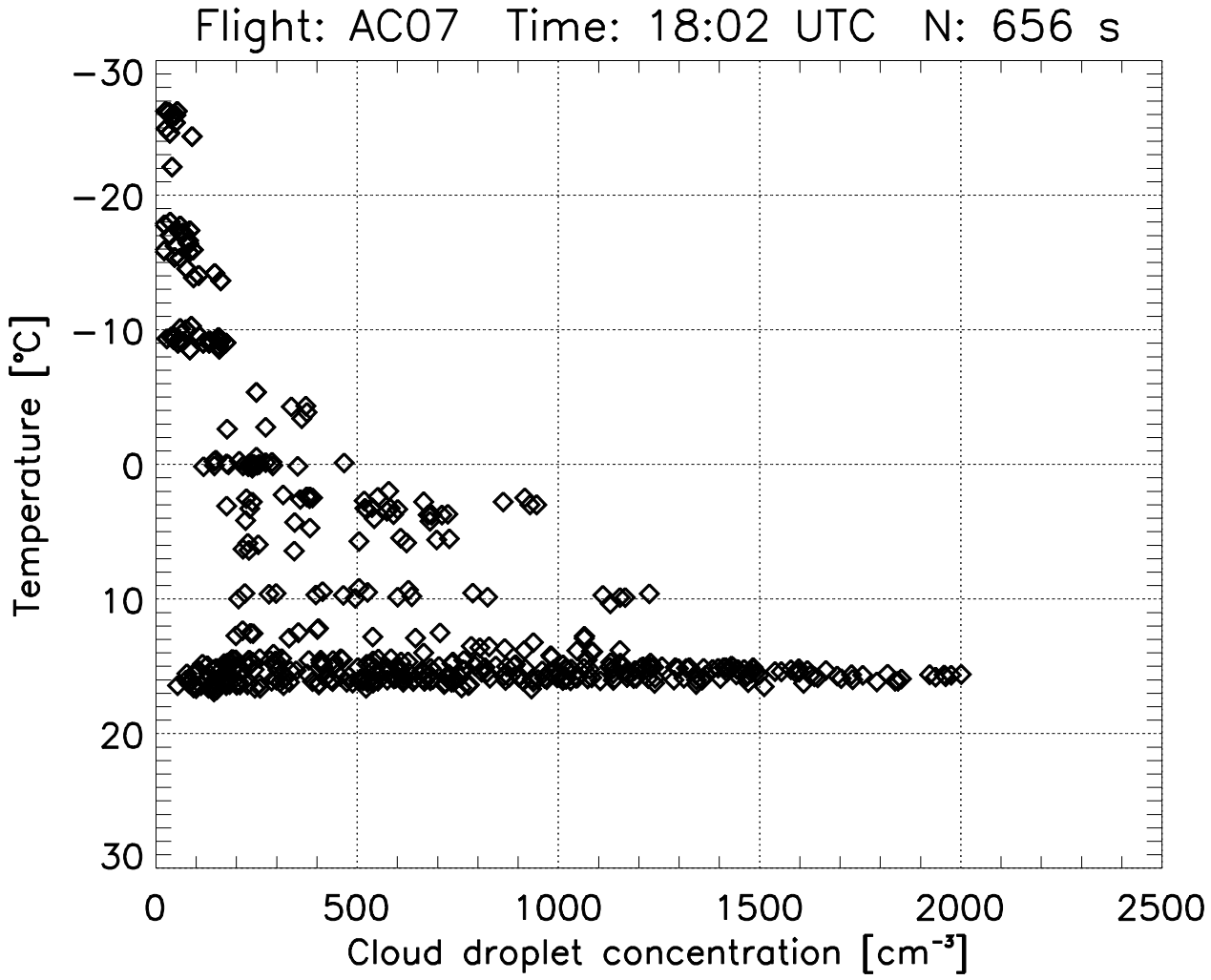

890 **Figure 5 Cloud droplet concentration measured with CCP-CDP as a function of temperature for flight AC07. Each dot indicates a 1-Hz average concentration. The sample number (N) and the approximate start time of the cloud profile are shown at the top of the panel.**

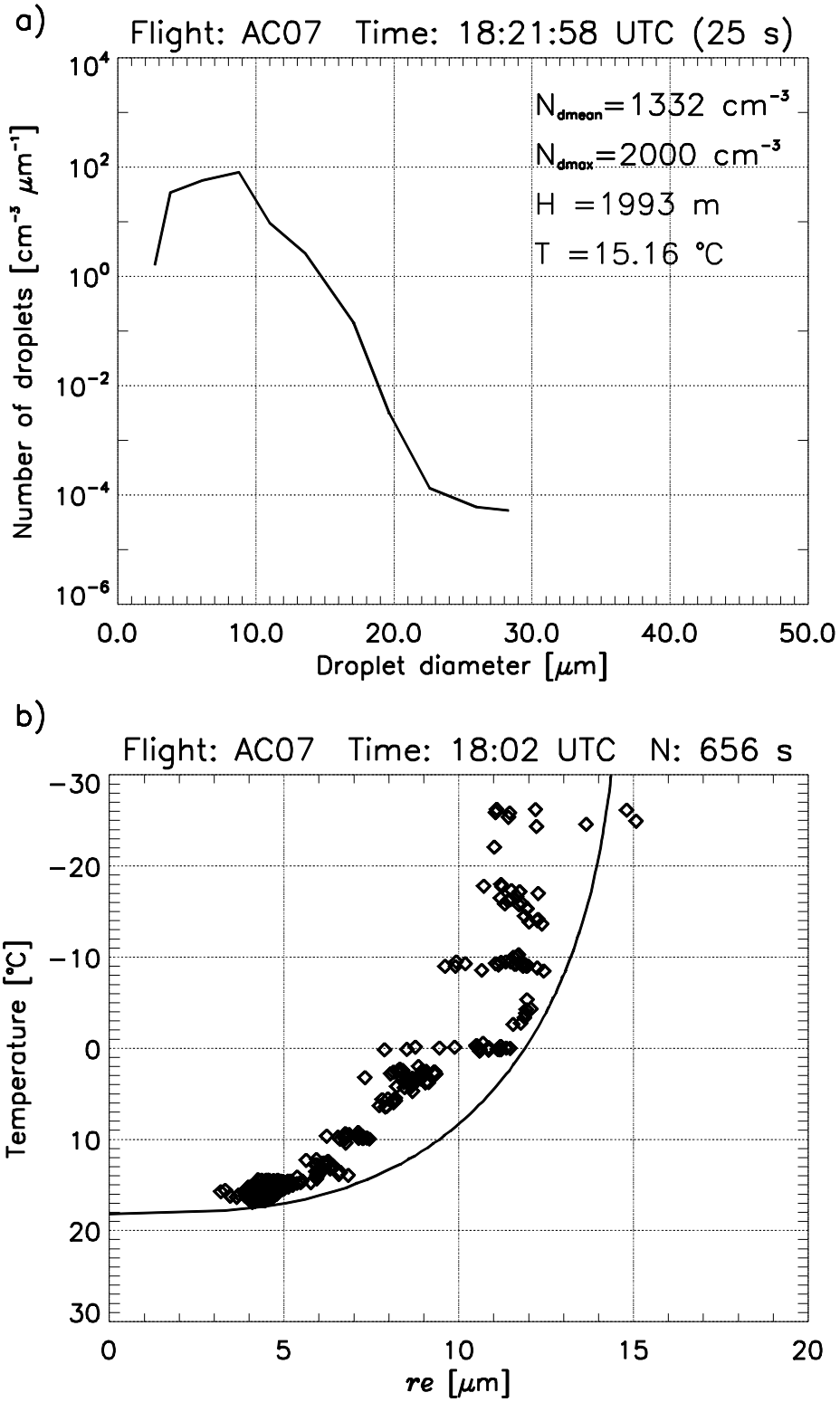

895 **Figure 6 a) Mean cloud droplet size distribution calculated from the CCP-CDP data for a cloud pass at cloud base during flight AC07. The flight number, initial time of cloud pass, and duration in seconds are shown at the top of graph. The mean total number of droplets (N_{dmean}), the maximum total number of droplets (N_{dmax}) in one second for this cloud pass, and the approximate height (H) and temperature (T) are shown at the upper-right corner of the graph; b) Cloud droplet effective radius (r_e) calculated from CCP-CDP as a function of tempera-**
900 **ture indicated with dots. The black line indicates the estimated adiabatic effective radius (r_{ea}) as a function of temperature.**

a)

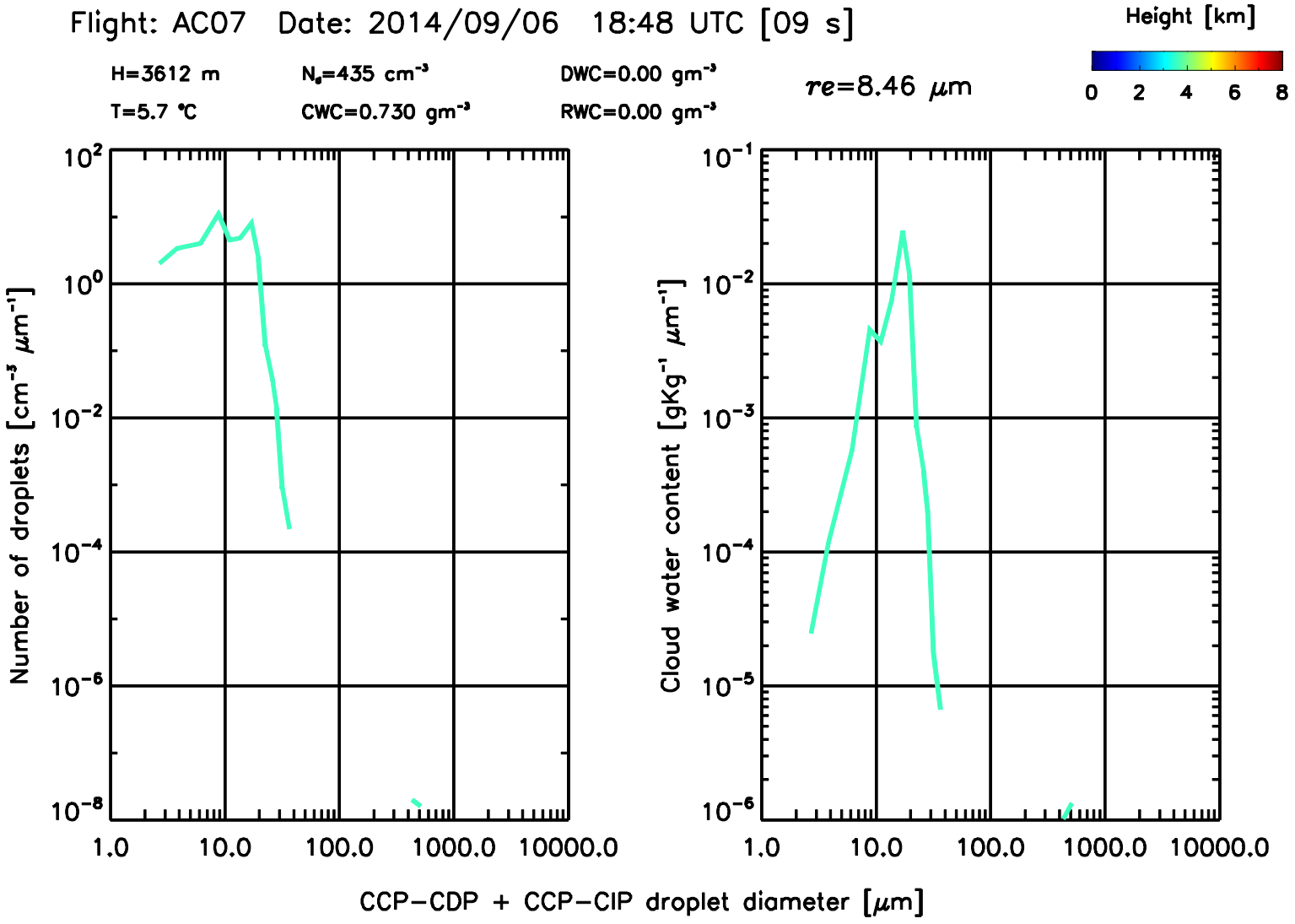
Flight: AC07 Date: 2014/09/06 18:48 UTC [09 s]
H=3612 m
T=5.7 °C
N_d=435 cm^{-3}
CWC=0.730 gm^{-3}
DWC=0.00 gm^{-3}
RWC=0.00 gm^{-3}
re=8.46 μm
Height [km]
0 2 4 6 8
Number of droplets [cm^{-3} μm^{-1}]
Cloud water content [gKg^{-1} μm^{-1}]
1.0 10.0 100.0 1000.0 10000.0
CCP−CDP + CCP−CIP droplet diameter [μm]

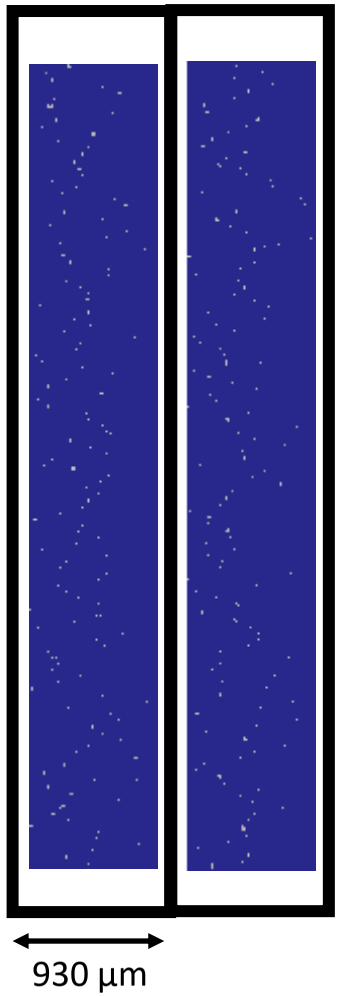
CCP-CIP Images
930 µm

b)

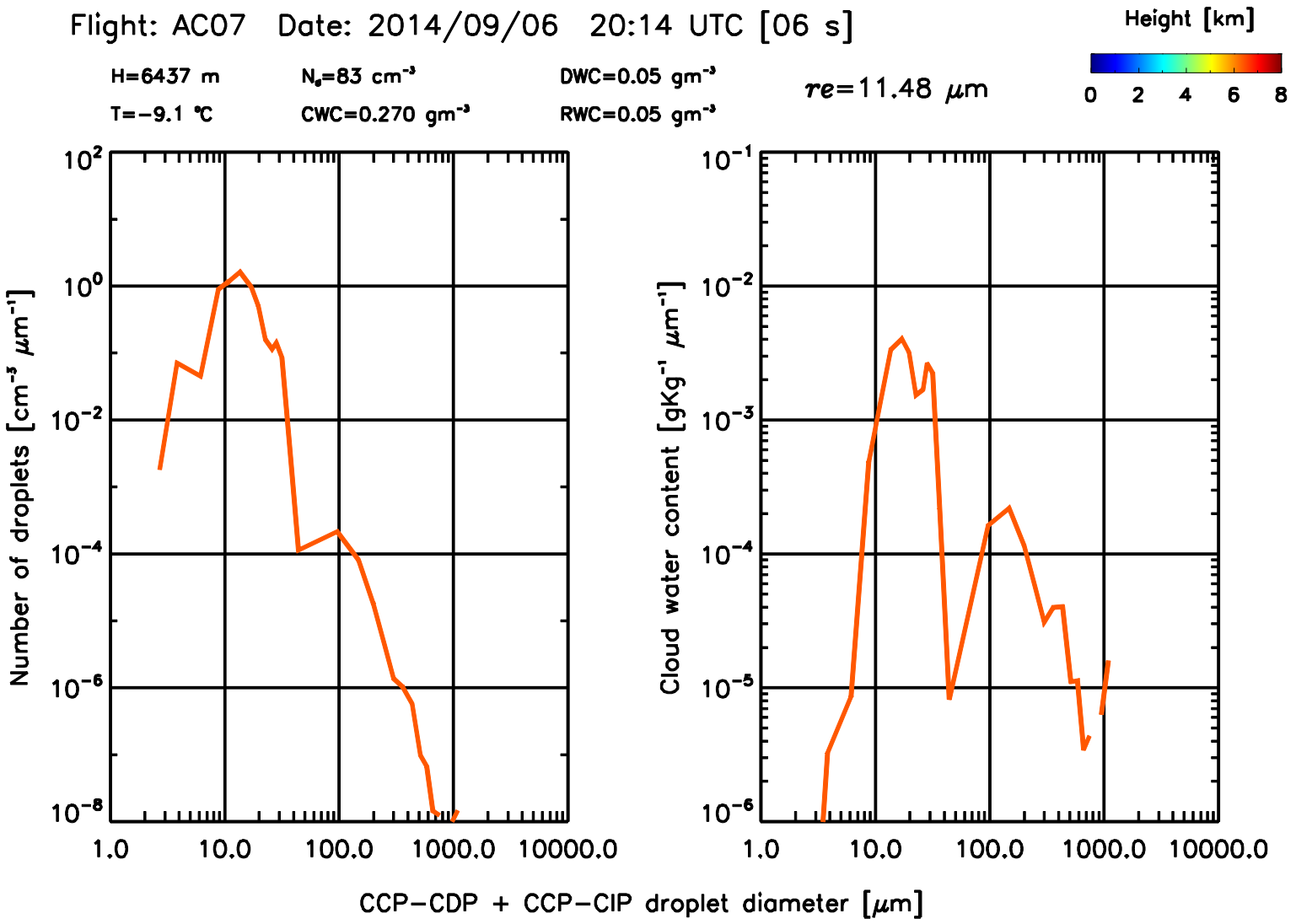
Flight: AC07 Date: 2014/09/06 20:14 UTC [06 s]
H=6437 m
T=−9.1 ℃
N_d=83 cm^{-3}
CWC=0.270 gm^{-3}
DWC=0.05 gm^{-3}
RWC=0.05 gm^{-3}
re=11.48 μm
Height [km]
0 2 4 6 8
Number of droplets [cm^{-3} μm^{-1}]
Cloud water content [gKg^{-1} μm^{-1}]
1.0 10.0 100.0 1000.0 10000.0
CCP−CDP + CCP−CIP droplet diameter [μm]

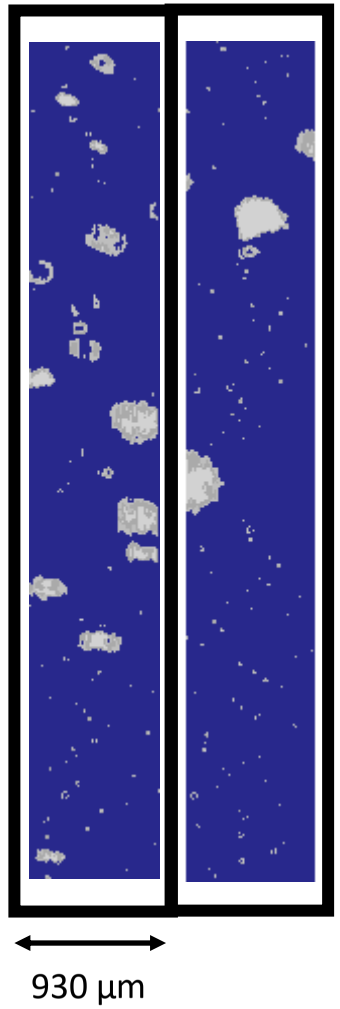
CCP-CIP Images
930 µm

c)

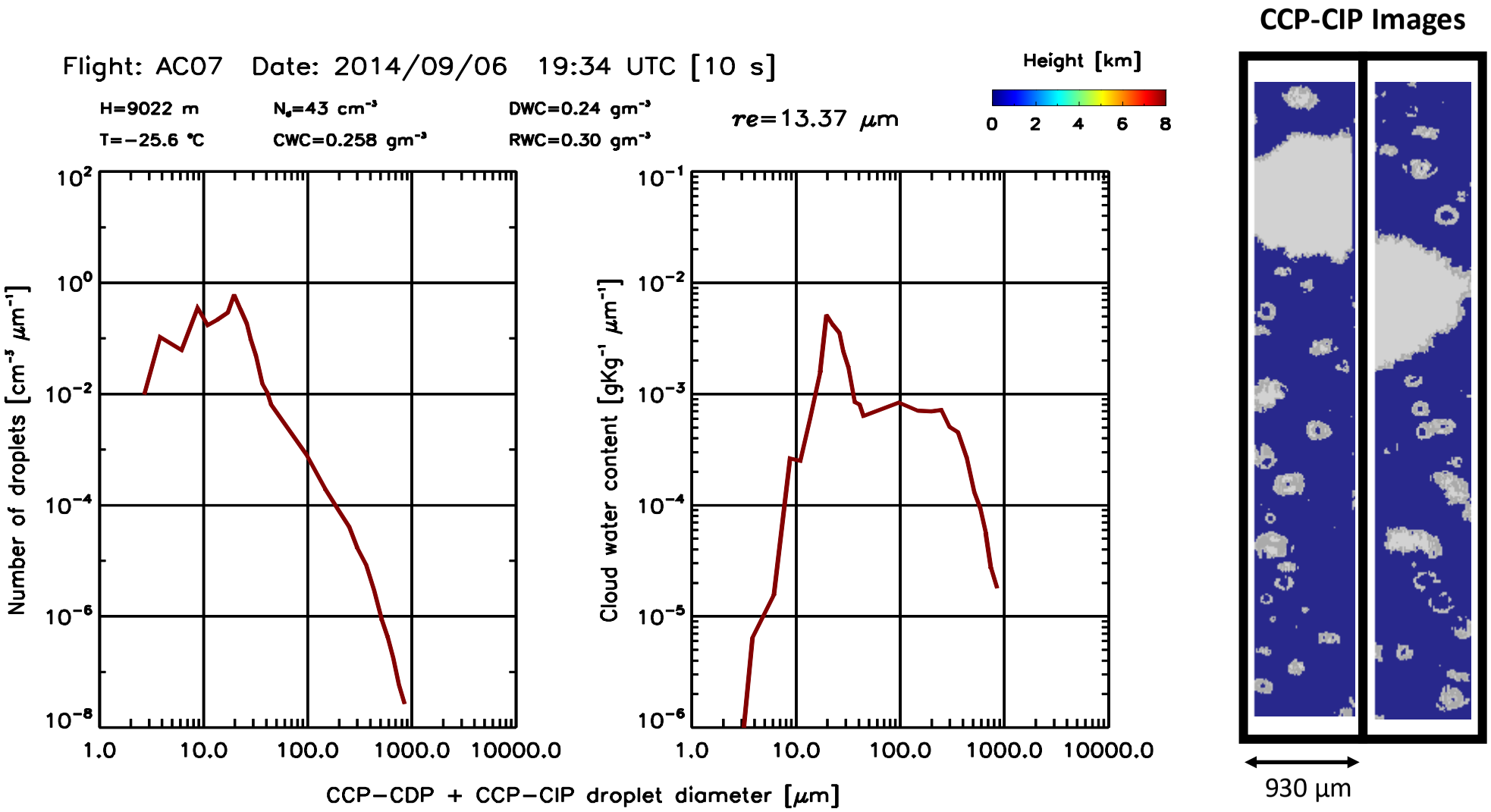

Figure 7a-c. Mean droplet size distribution composite from the CCP-CDP and CCP-CIP probes (left panel). Similar for indicated cloud water content in the right panel. Indicated at the top of the panels are the HALO flight number, date, time of flight (UTC), duration of cloud pass in seconds, temperature (T) and altitude (H) above sea level, and the mean values for the total number of droplets (N_d), CWC, DWC, RWC, and r_e. The color bars indicate the height of HALO during the cloud pass. On the right side of the panels CCP-CIP images corresponding to the cloud pass are shown.

Figure 8 Image taken from the HALO cockpit just before the aircraft penetration of a convective cloud with lightning activity during flight AC07. In this case, the cloud pass height was 9,022 m (temperature ~ -25 ºC) and the maximum CWC measured was 0.55 g m^{-3}.

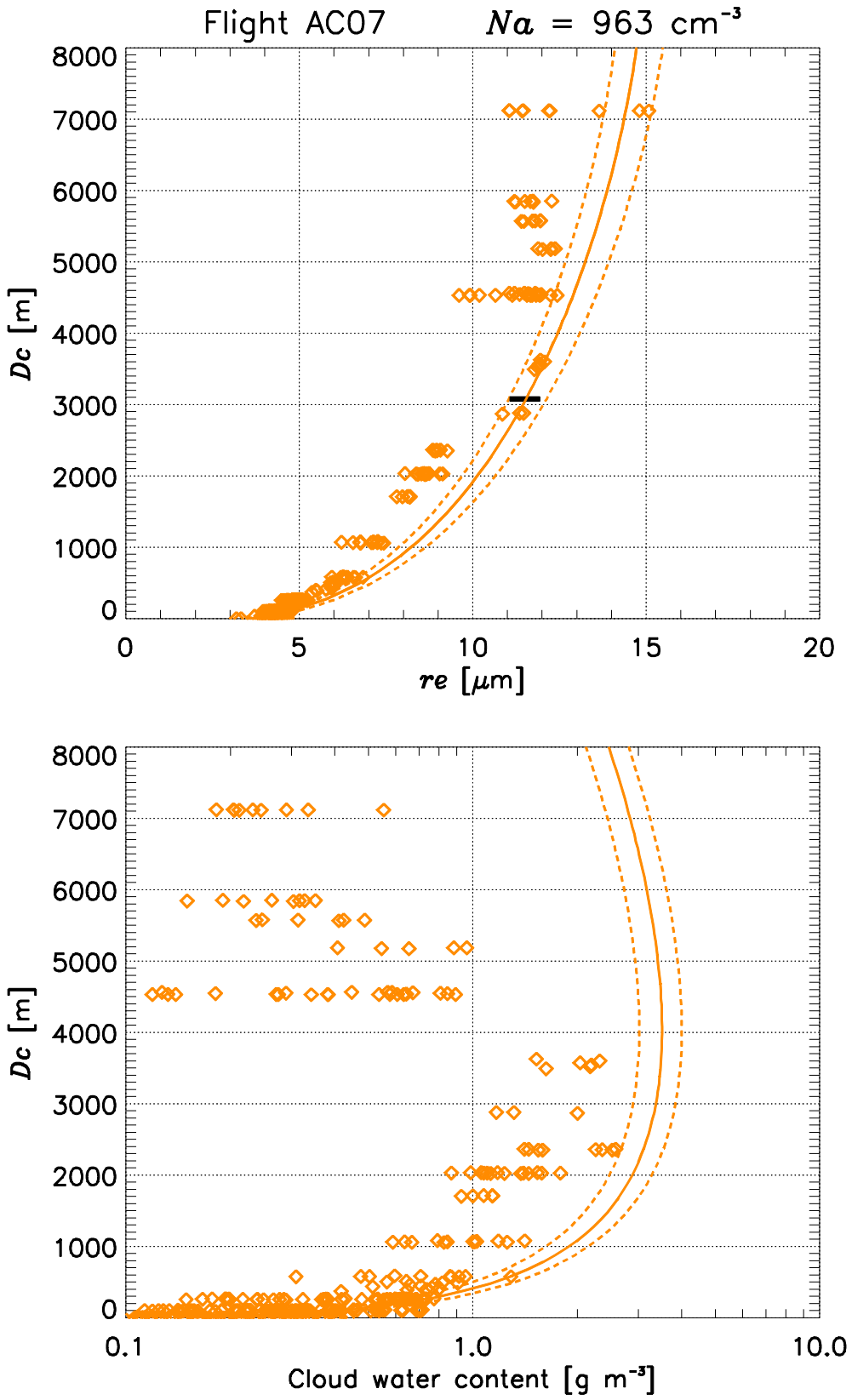

Figure 9 a) Cloud droplet effective radius (r_e) as a function of cloud depth (D_c) for flight AC07. The line indicates the r_e estimated for adiabatic growth (r_{ea}) from cloud base (dashed lines indicate the r_{ea} values considering the uncertainty of the estimate). The height of 0 °C is indicated by a black horizontal bar across the r_{ea} line. The estimated adiabatic number of droplets (N_a) at cloud base is shown at the top of the figure. b) Similar to a) for Cloud water content (adiabatic values are shown by lines).

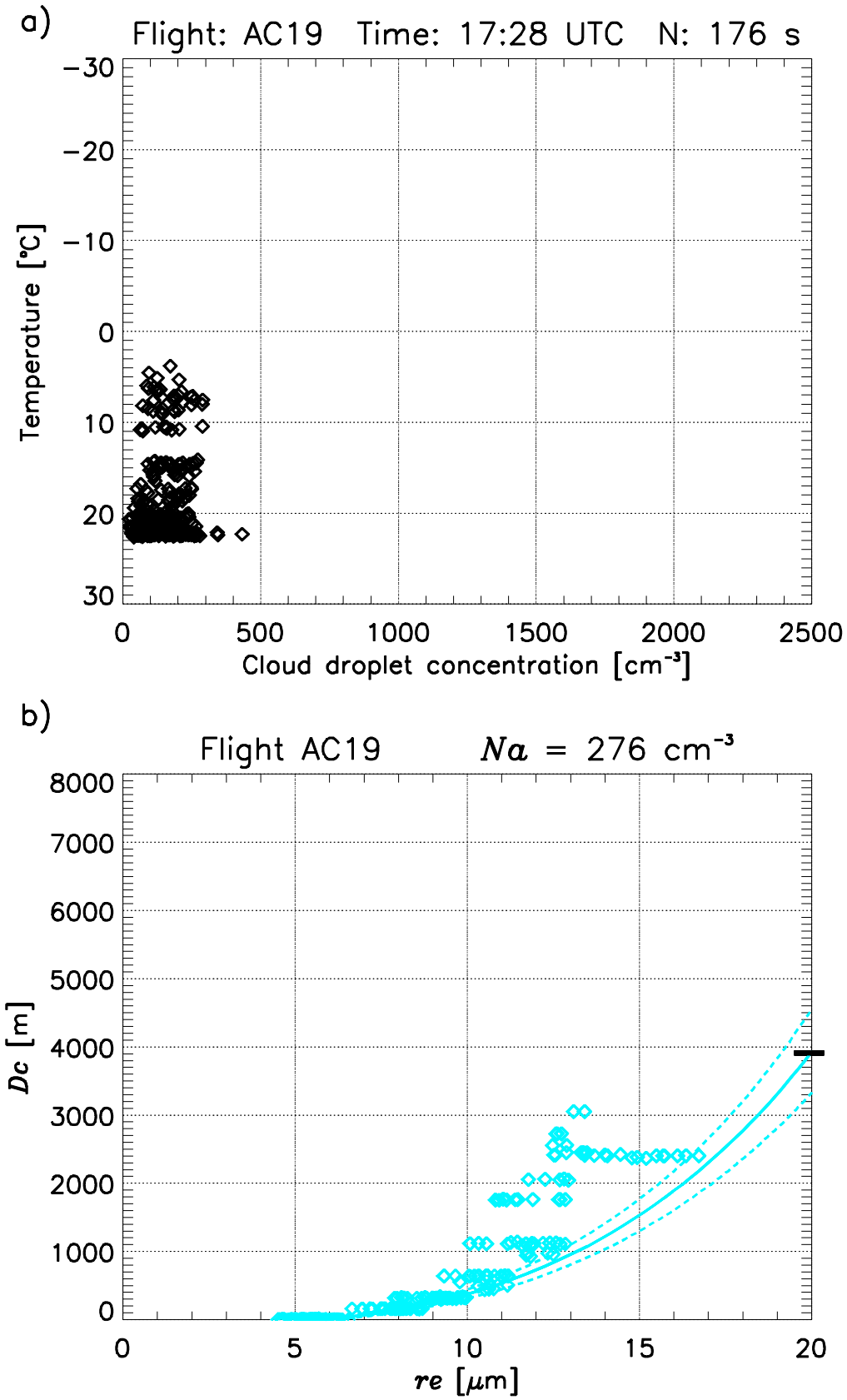

Figure 10 a) Cloud droplet concentrations measured with the CCP-CDP as a function of temperature for flight AC19. Each dot indicates 1Hz average concentration. The sample number in seconds (N) and the start time of the cloud profile are shown at the top of the panel; b) Similar to Figure 9 for flight AC19.

a)

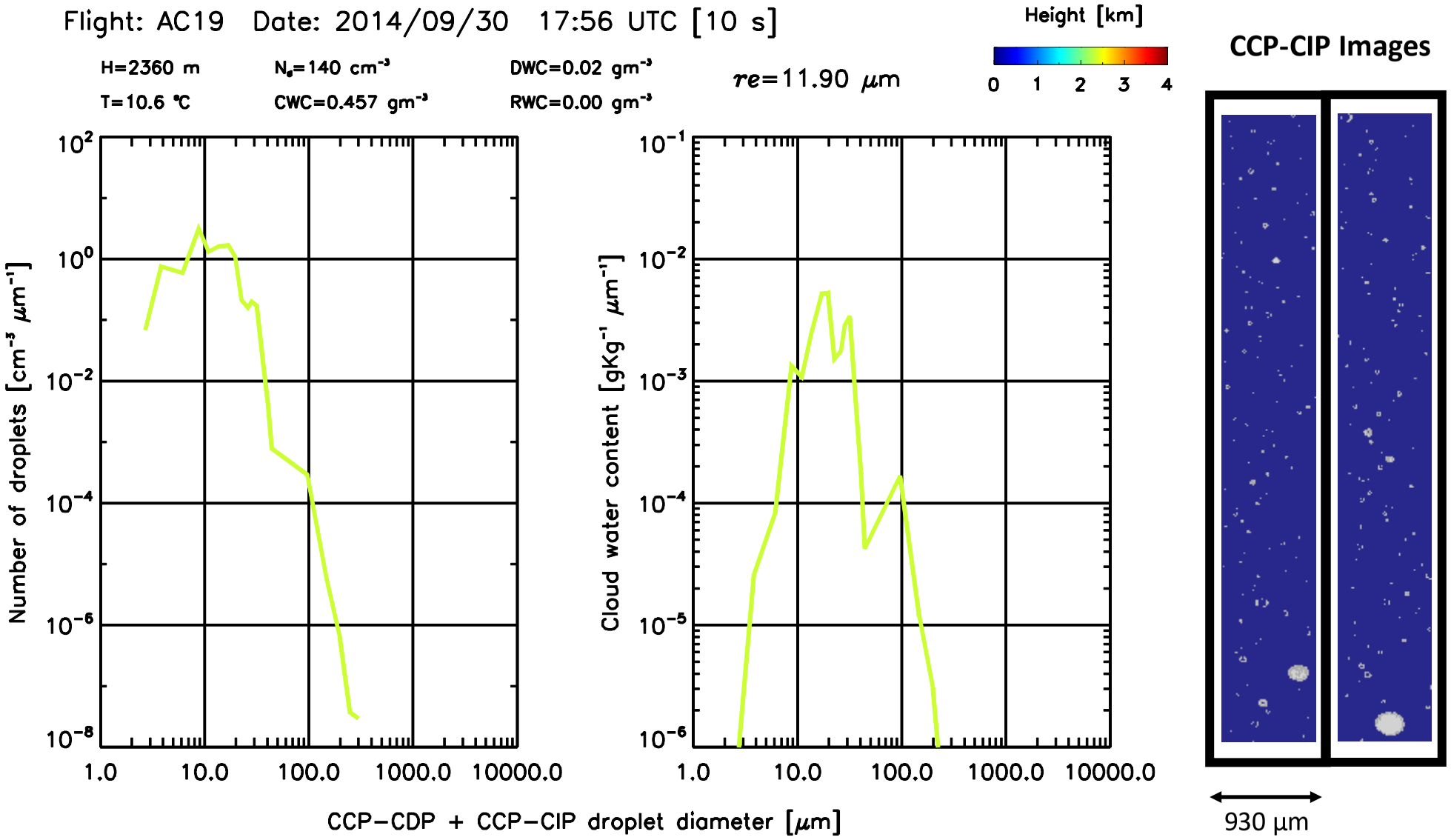
Flight: AC19 Date: 2014/09/30 17:56 UTC [10 s]
H=2360 m
T=10.6 °C
N_c=140 cm^{-3}
CWC=0.457 gm^{-3}
DWC=0.02 gm^{-3}
RWC=0.00 gm^{-3}
re=11.90 μm
Height [km]
0 1 2 3 4
CCP-CIP Images
Number of droplets [cm^{-3} μm^{-1}]
Cloud water content [gKg^{-1} μm^{-1}]
1.0 10.0 100.0 1000.0 10000.0
CCP−CDP + CCP−CIP droplet diameter [μm]
930 μm

b)

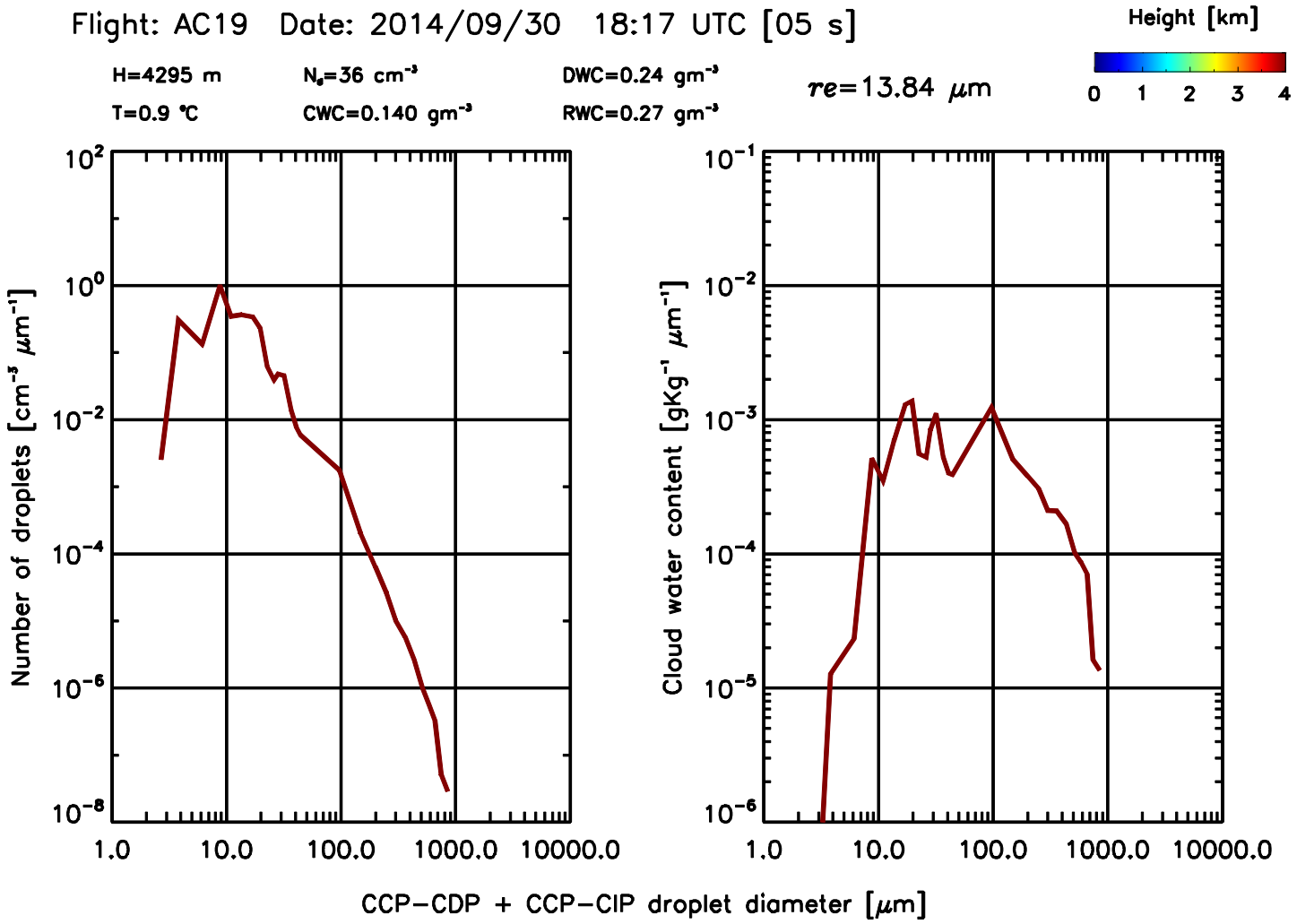

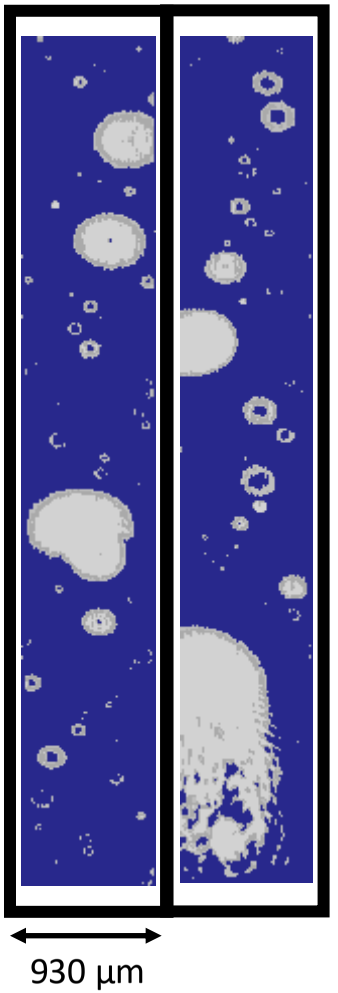

Figures 11 a-b) Similar to Figures 7a-c for flight AC19.

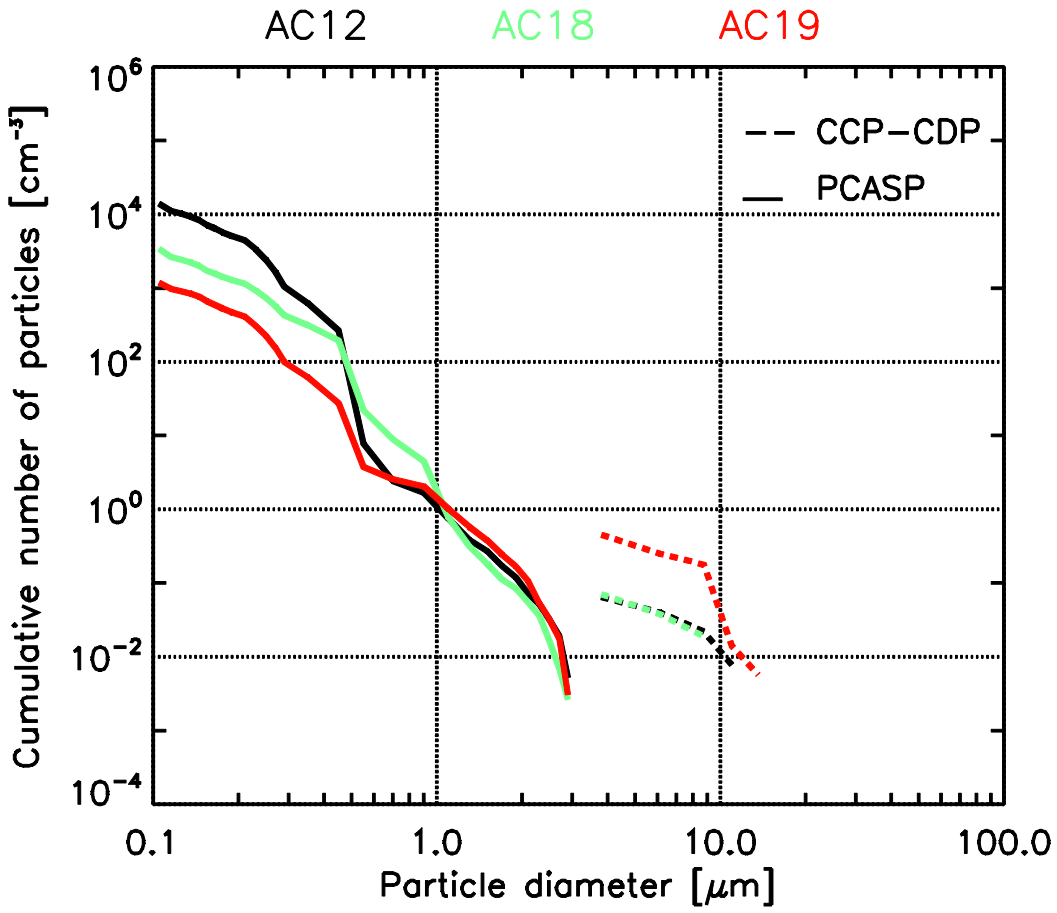

Figure 12 Cumulative aerosol size distribution below cloud base calculated from the PCASP probe for typical clean, polluted, and very polluted regions (solid line) for flights AC12 (very polluted), AC18 (polluted), and AC19 (clean). Similar for cumulative cloud droplet size distribution calculated with CCP-CDP (dashed line). The flight numbers are indicated by colors at the top of the panel.

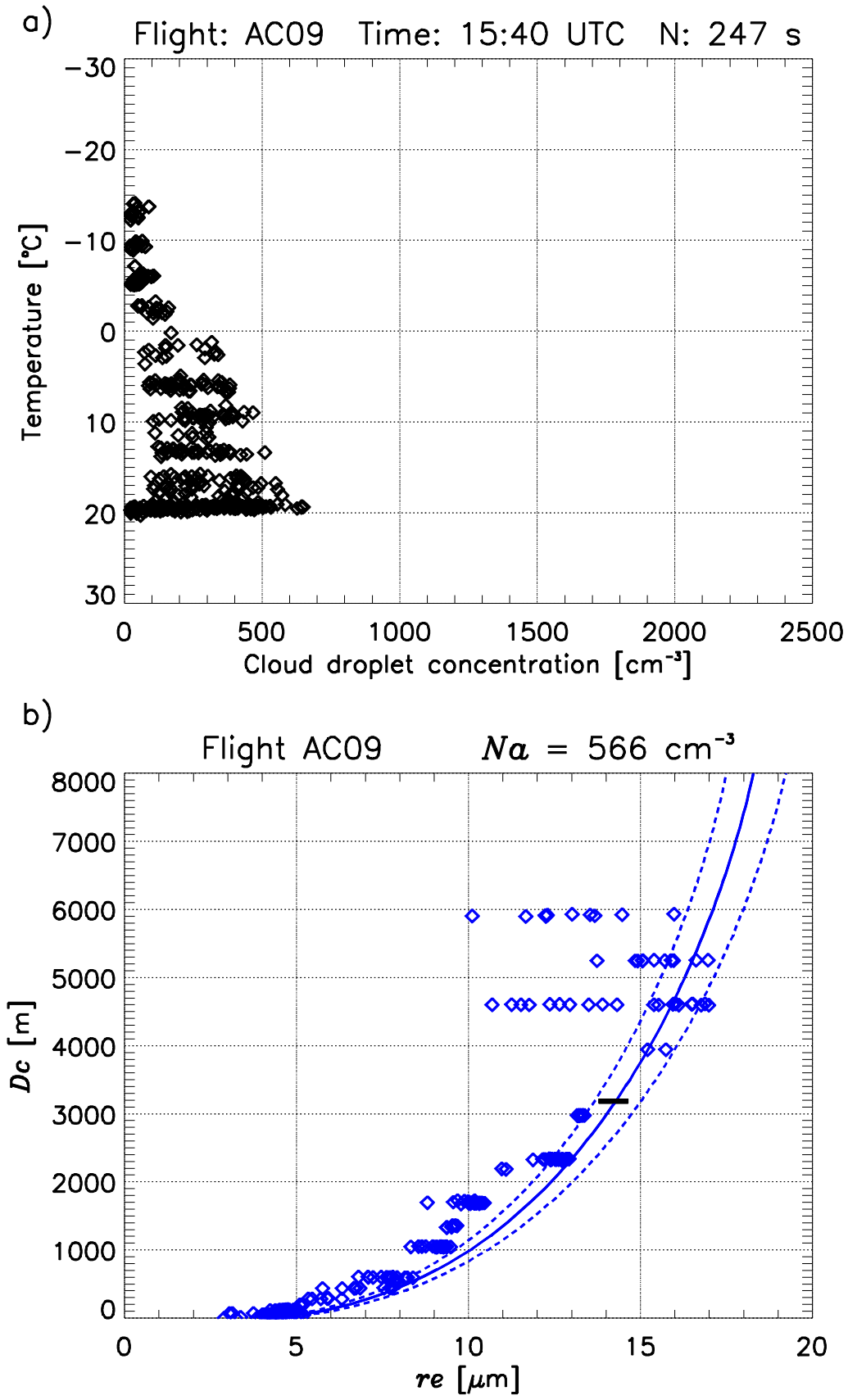

Figure 13 a) Cloud droplet concentrations measured with the CCP-CDP as a function of temperature for flight AC09. Each dot indicates 1-Hz average concentration. The sample number in seconds (N) and the start time of the cloud profile are shown at the top of the panel; b) Similar to Figure 9 for flight AC09.

a)

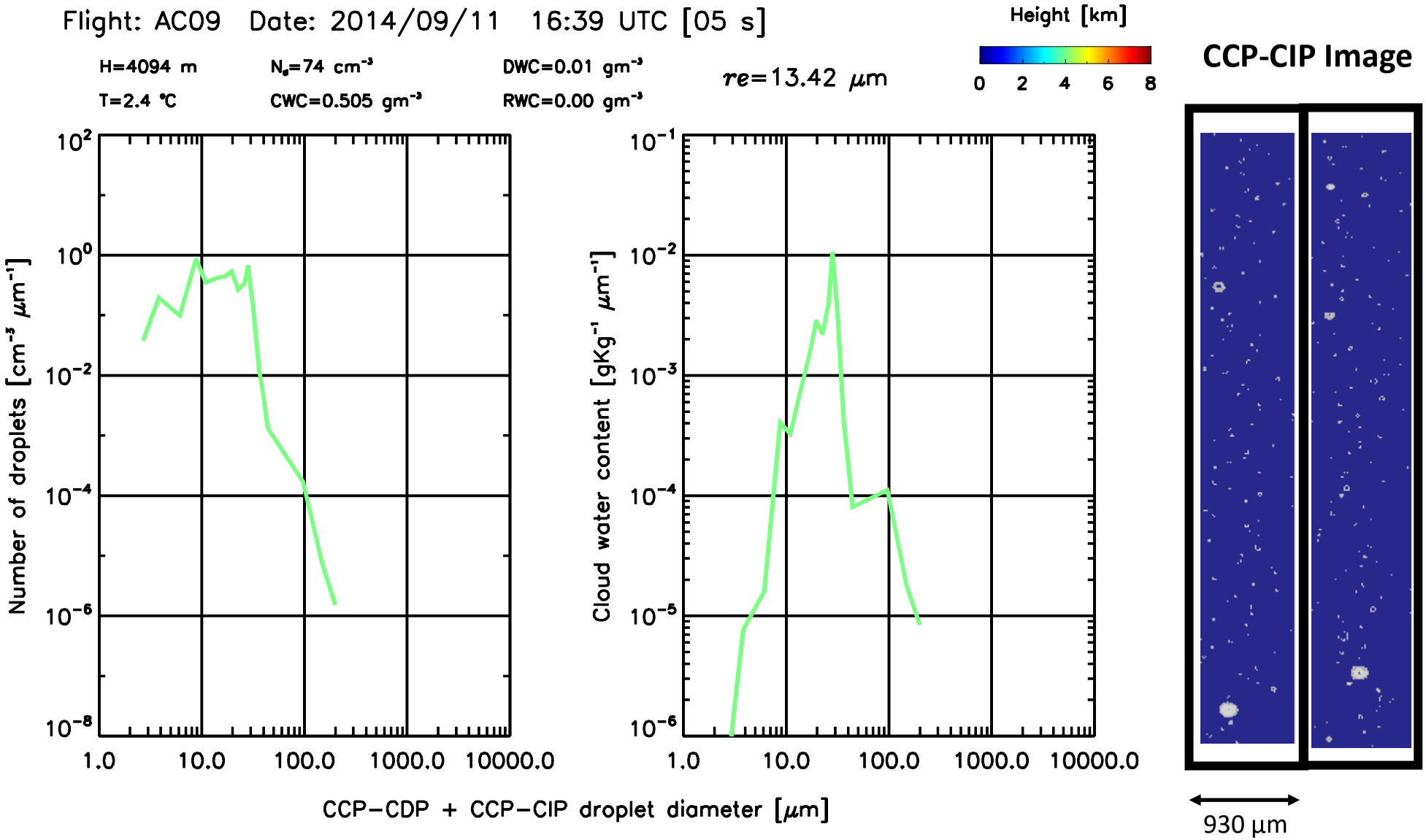
Flight: AC09 Date: 2014/09/11 16:39 UTC [05 s]
H=4094 m
T=2.4 °C
N_c=74 cm^{-3}
CWC=0.505 gm^{-3}
DWC=0.01 gm^{-3}
RWC=0.00 gm^{-3}
re=13.42 μm
Height [km]
0 2 4 6 8
CCP-CIP Image
Number of droplets [cm^{-3} μm^{-1}]
Cloud water content [gKg^{-1} μm^{-1}]
1.0 10.0 100.0 1000.0 10000.0
CCP−CDP + CCP−CIP droplet diameter [μm]
930 μm

b)

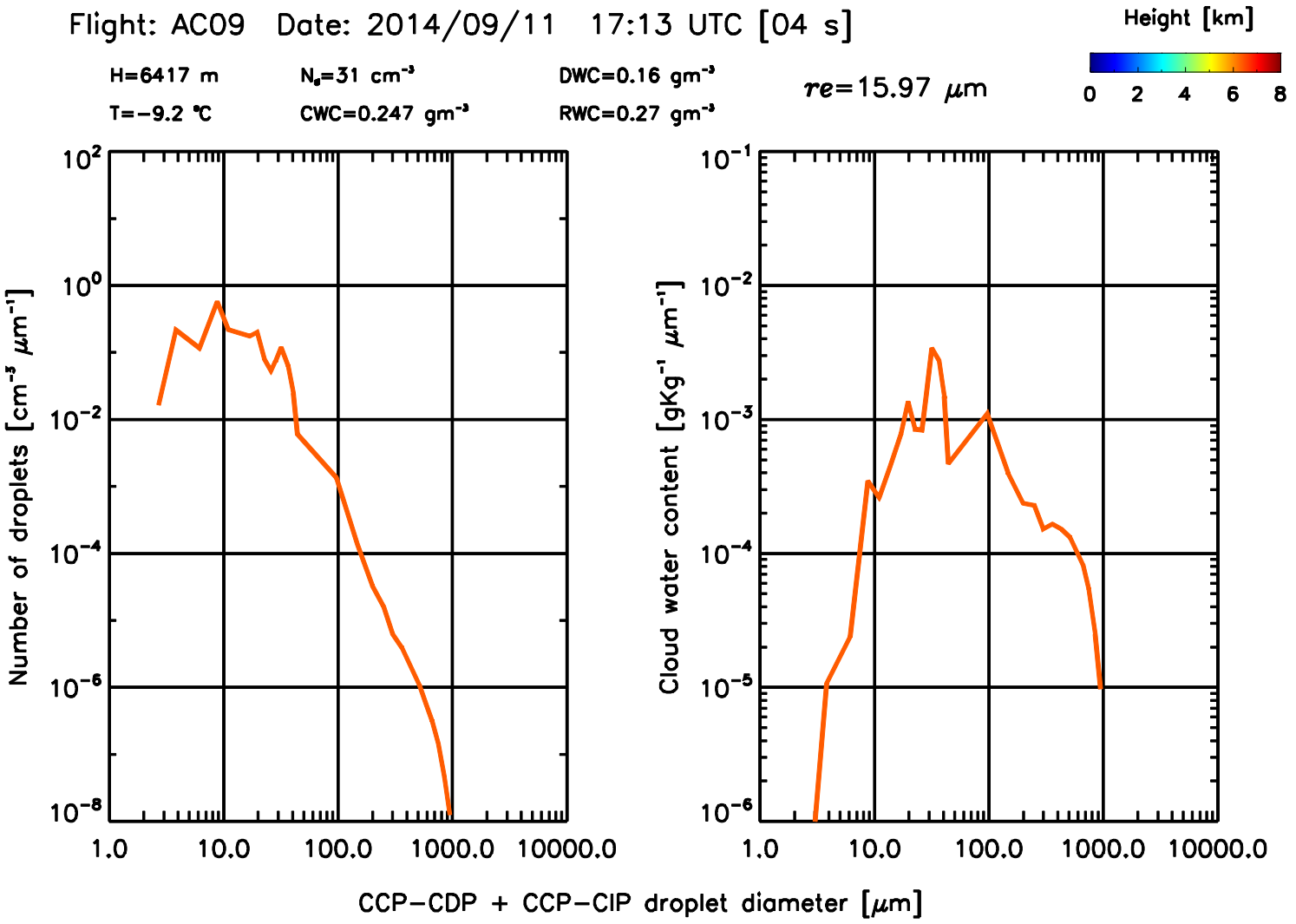

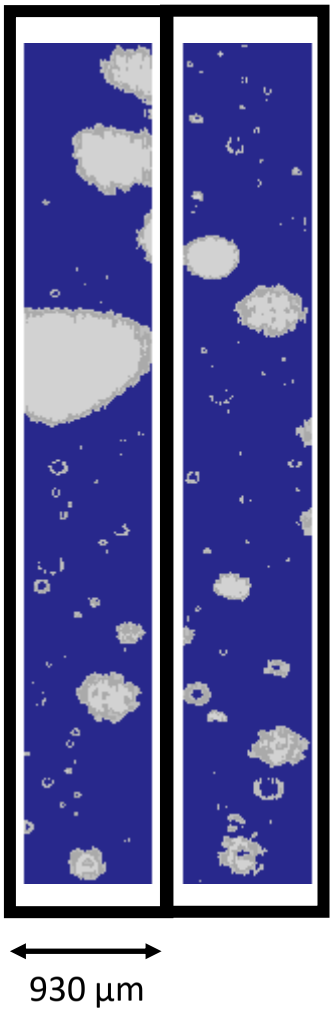

Figures 14 a-b) Similar to Figures 7a-c for flight AC09.

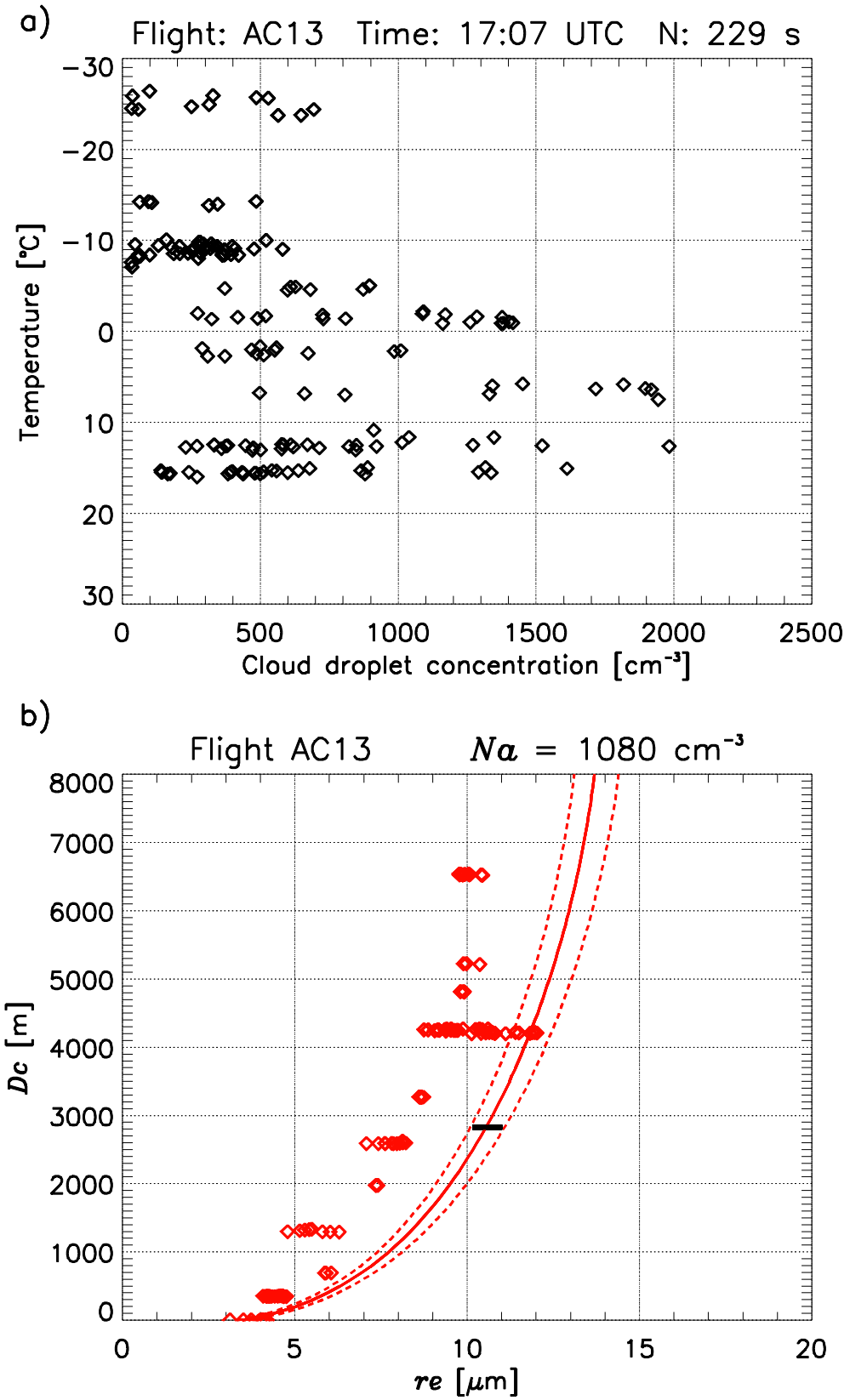

Figure 15 a) Cloud droplet concentration measured with the CCP-CDP probe as a function of temperature for flight AC13. Each dot indicates a 1-Hz average concentration. The sample number and the approximate time of the cloud profile are shown at the top of the panel; b) Similar to figure 9 for Flight AC13.

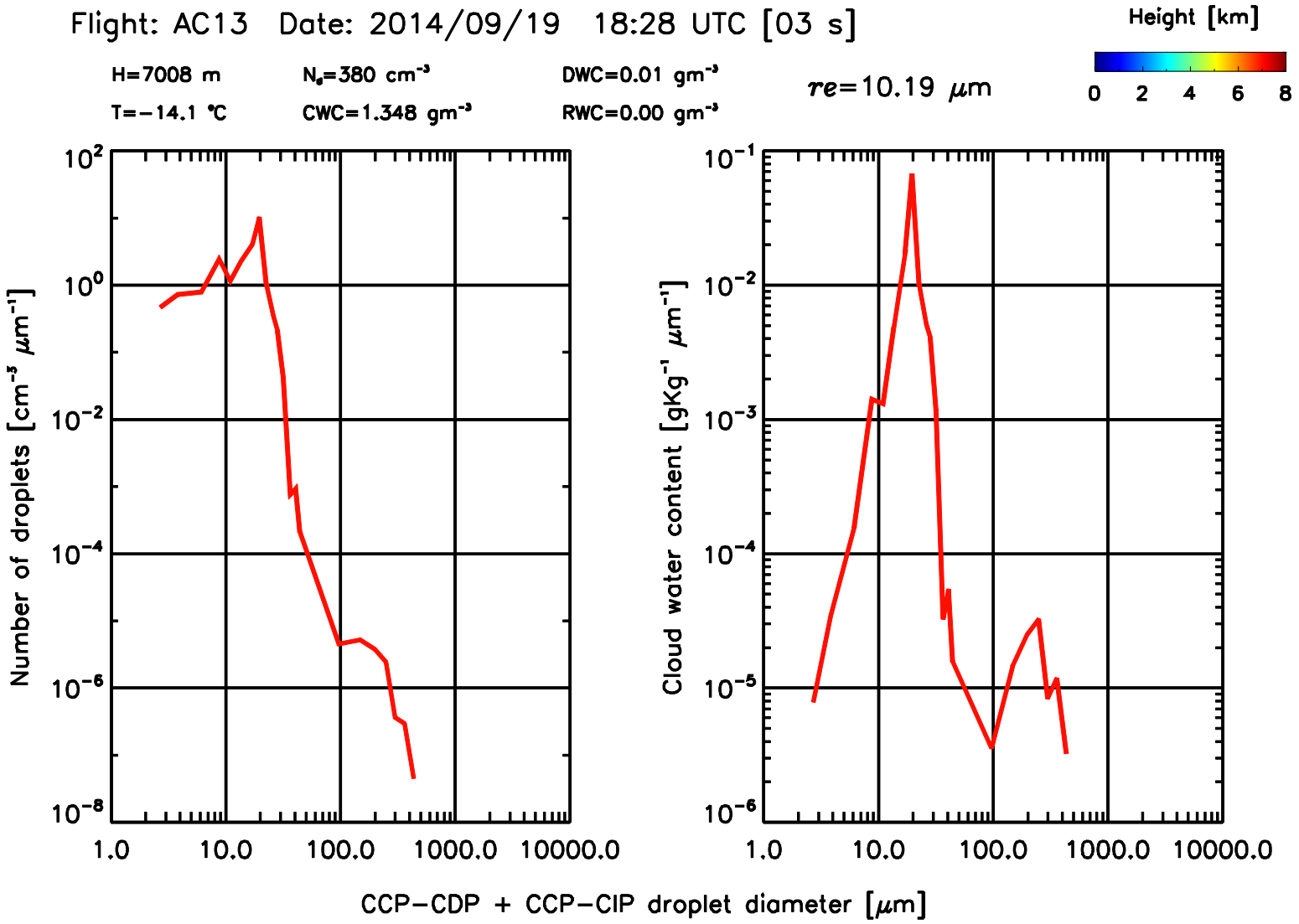

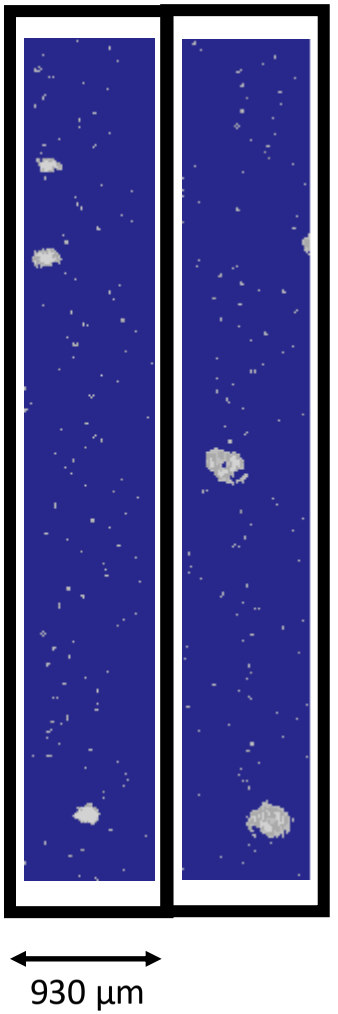

Figures 16 Similar to Figures 7a-c for flight AC13.

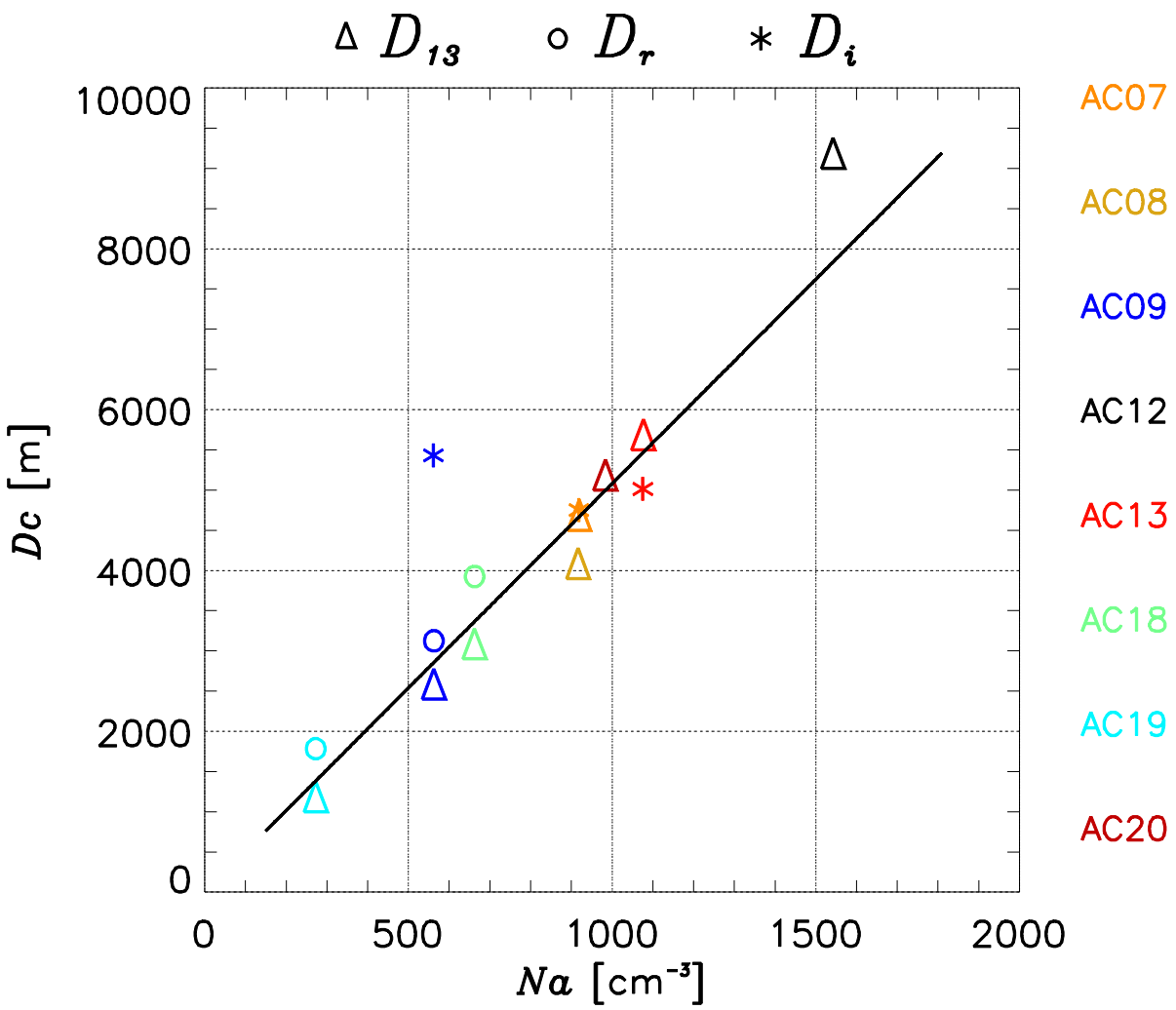

Figure 17 Cloud depth (D_c) as a function of the estimated adiabatic number of droplets (N_a) at cloud base. D_c for adiabatic cloud droplet effective radius (r_{ea}) equal 13 µm (or D_{13}) are indicated by triangles. Similar for cloud depth of rain initiation (D_r) [indicated by circles] and cloud depth for ice initiation (D_i) [indicated by asterisk]. The flight numbers are indicated by colors on the right side of the panel. The values of D_{13}, D_r, and D_i are shown in Table 1. The black line indicates the linear equation for D_{13} as a function of N_a for all flights, where: $D_r = (5\pm0.7)N_a$

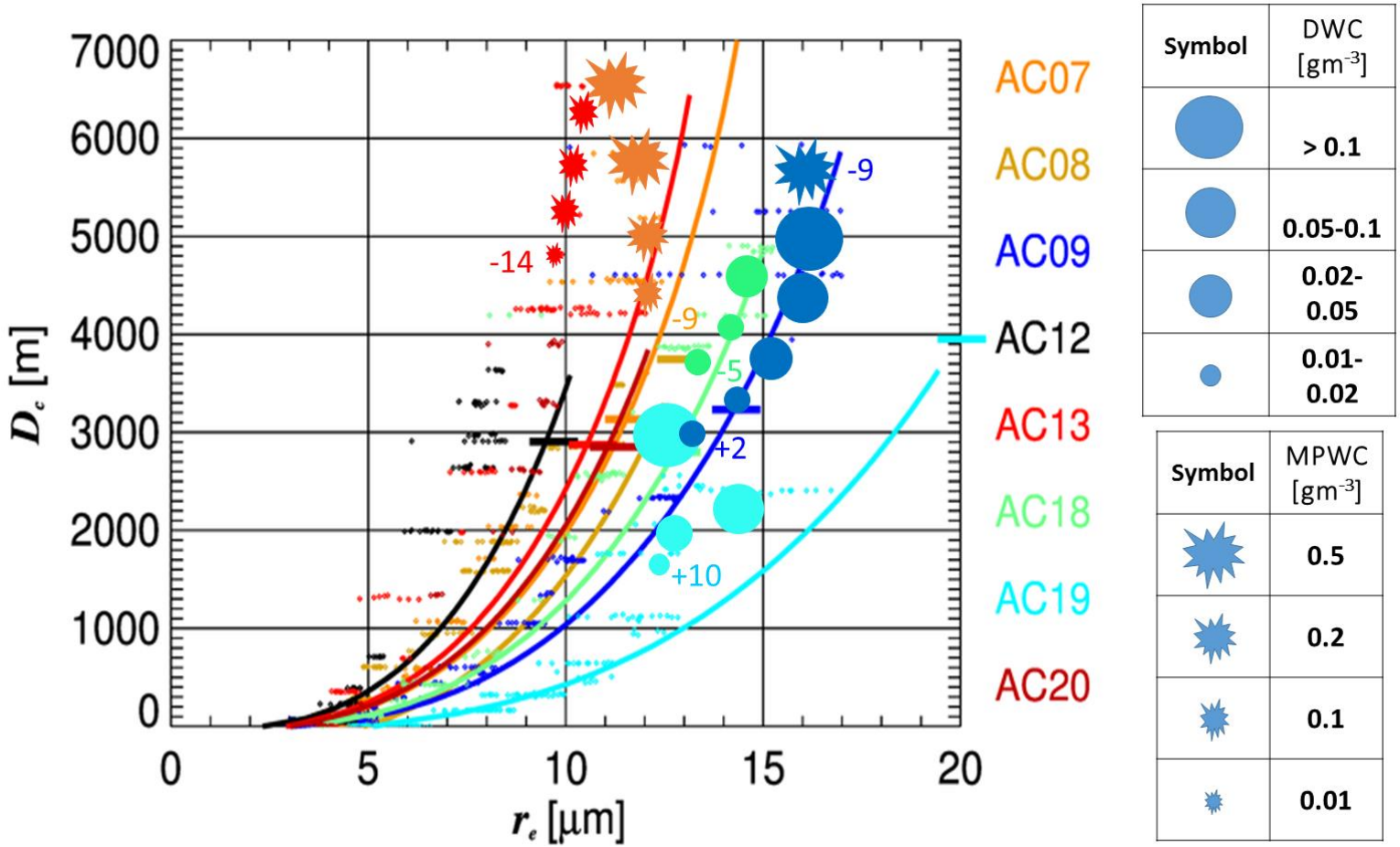

Figure 18 CDP-measured cloud droplet effective radius (r_e) (colored dots) and estimated cloud droplet adiabatic effective radius (r_{ea}) (colored lines) as a function of cloud depth (D_c) for all flights (indicated by colors). The height of 0 °C is indicated by a horizontal bar across the r_{ea} line. The circles indicate the approximate values of drizzle water content (DWC) calculated from the CCP-CIP data, the range of DWC values is indicated in the table at the upper-right side of the figure. The star symbols indicate approximate mixed phase drizzle water content (MPWC) values calculated from the CCP-CIP data (indicated in the table at the bottom-right side of the figure). The temperature in °C of rain or ice initiation (D_r and D_i, respectively) is indicated by colored numbers close to the circle or star symbols.